Theoretical calculation of equilibrium Mg isotope fractionations between minerals and aqueous solutions

Caihong Gao[a,b], Xiaobin Cao[c], Qi Liu[a], Yuhong Yang[d], Siting Zhang[d], Yuyang He[c], Mao Tang[a], Yun Liu[a,*]

[a] State Key Laboratory of Ore Deposit Geochemistry, Institute of Geochemistry, Chinese Academy of Sciences, Guiyang 550081, China
[b] University of Chinese Academy of Sciences, Beijing 100049, China
[c] Department of Geology & Geophysics, Louisiana State University, USA
[d] Lunar and Planetary Science Research Center, Institute of Geochemistry, Chinese Academy of Sciences, Guiyang 550081, China

ARTICLE INFO

ABSTRACT

There are large discrepancies existing in equilibrium Mg isotope fractionation calculations and experimental investigations for cases related to mineral vs. solution. To clarify this confusing issue, a newly designed cluster-model-based quantum chemistry method, i.e., volume variable cluster model (VVCM), is used to provide equilibrium Mg isotope fractionation factors between Mg-bearing carbonates (calcite, aragonite, dolomite and magnesite), amorphous calcium carbonates (ACCs), brucite and aqueous species (i.e., $Mg^{2+}_{(aq)}$, $MgHCO_3^+_{(aq)}$ and $MgOH^+_{(aq)}$). We find that local configuration sampling of aqueous species is essential to provide precise fractionations between mineral and solution. The phonon-based periodic boundary method is also used for several minerals and it obtains very similar fractionations with VVCM results.

Our results are very close to those of Pinilla et al. (2015) although via completely different approaches. Both of them have included the effect of local configuration disorder. However, both of them are significantly different from some of experimental results for cases of carbonates vs. solutions. The existence of various Mg-bearing species in fluids of experiments, the direct incorporation of hydrated Mg^{2+} into the solids, the Mg^{2+} concentration effect, and the existence of intermediate precursors (e.g., ACCs) are several possible causes for the mismatches. Relative to coexisting aqueous Mg^{2+}, we find that ACCs will enrich heavy Mg isotopes, i.e., ~1.45‰ at 25 °C, agreeing with previous experimental estimation. Equilibrium Mg isotope fractionation factors between brucite and solutions are also predicted. Besides, we applied VVCM to predict the Mg isotope fractionations between high-temperature phases, i.e., forsterite, diopside, enstatite, tremolite and spinel. The predicted β factors are in the order of spinel > tremolite > diopside > enstatite > forsterite. This study provides a base for understanding the accumulating Mg isotope data.

1. Introduction

Magnesium is one of the most abundant elements in silicate earth. Equilibrium Mg isotope fractionations are significant (> 8‰, hereafter in terms of $^{26}Mg/^{24}Mg$) because of relatively large mass difference between ^{24}Mg and ^{26}Mg. Due to recent developments in mass spectrometry, Mg isotopes have provided useful information for various geological investigations (Teng, 2017), such as paleo-environment reconstruction (e.g., Buhl et al., 2007), chemical weathering (e.g., Tipper et al., 2006, 2012a, 2012b; Shen et al., 2009; Teng et al., 2010; Huang et al., 2012), upper mantle properties (e.g., Teng et al., 2007; Wiechert and Halliday, 2007; Handler et al., 2009), plant growth (e.g., Black et al., 2006, 2007, 2008; Bolou-Bi et al., 2010) and early solar systems

evolution (e.g., Galy et al., 2000; Baker et al., 2012; Davis et al., 2015). Such applications require an extensive determination of equilibrium Mg isotope fractionation data.

Equilibrium Mg isotope fractionations between carbonates and co-existing solutions have been investigated by experiments (e.g., Immenhauser et al., 2010; Pearce et al., 2012; Saulnier et al., 2012; Li et al., 2012, 2015; Mavromatis et al., 2013, 2017; Wang et al., 2013), but there are about 1‰–2‰ discrepancies existing among those studies. On the other hand, Rustad et al. (2010) performed embedded-cluster-based quantum chemistry calculations to determine equilibrium Mg isotope fractionations between carbonates and aqueous Mg^{2+} ion. Meanwhile, Schauble (2011) used phonon-based periodic boundary density functional perturbation theory (DFPT) method to calculate

---

isotope fractionations between carbonate minerals and hexa-aqua-magnesium (2 +) crystal. These two theoretical predictions are not only significantly different from each other, but also largely different from experimental results (Pearce et al., 2012; Li et al., 2015).

To resolve these controversies, Pinilla et al. (2015) conducted a study on Mg isotope fractionations between carbonate minerals and aqueous Mg^{2+}. They used path integral molecular dynamics (PIMD) and Car-Parrinello molecular dynamics (CPMD) for aqueous Mg^{2+}. They performed local configurational disorder sampling for the aqueous Mg^{2+}. For solid phases, they fixed the lattice parameters as experimental values and only optimized atomic positions to correct systematic errors. This treatment will put small artificial stress on the structures (Wang et al., 2017) and may not completely correct the systematic errors (Blanchard et al., 2017). Interestingly, the DFT-based results of Pinilla et al. (2015) generally support those of cluster-model-based method (i.e., Rustad et al., 2010) but largely different from another DFT-based study (i.e., Schauble, 2011).

The discrepancies between theoretical and experimental studies have not been well explained. It was suggested that the discrepancy in the case of magnesite vs. aqueous Mg^{2+} was aroused from the existence of other Mg-bearing species (e.g., $MgHCO_3^+$ and $MgCO_3^0$) (Schott et al., 2016). However, it cannot explain some very large discrepancies in calcite- and aragonite-related cases. Meanwhile, the occurrence of amorphous calcium carbonate (ACC) precursors during non-classical growth stages of carbonates may have significant effects on isotope fractionation. Mavromatis et al. (2017) reported temporal evolution of Mg isotope fractionations between ACCs and solutions during calcite precipitation process. They found that Mg-ACC solids have heavier Mg isotope composition relative to aqueous Mg^{2+} by ~0–2‰. However, there is no theoretical equilibrium Mg isotope fractionation factors reported for Mg-bearing ACCs to date.

Brucite often occurs as a secondary mineral in contact metamorphic zone between dolomite and magmatic intrusion (Brown et al., 1985). It has layered structure with Mg^{2+} occupied octahedral site, which is thought to be an analogue for the octahedral layers in clay minerals (Harder, 1972). Knowing Mg isotope fractionations between brucite and coexisting solutions would provide important implications for the processes of weathering and alteration of silicate rocks (Li et al., 2014). Wimpenny et al. (2014) performed an experimental study and suggested that brucite enriched heavier Mg isotope composition relative to coexisting solution. However, another experimental study suggested an opposite direction (Li et al., 2014). On the other hand, Colla et al. (2018) used embedded cluster method to predict Mg isotope fractionation between brucite and aqueous Mg^{2+}. They reported positive but much larger isotope fractionation values.

In this study, we provide equilibrium Mg isotope fractionation factors for Mg-bearing minerals, ACCs and aqueous solutions. By comparing our results with previous ones, we can obtain some insights on the possible reasons of those discrepancies.

2. Methods

2.1. Equilibrium isotope fractionation theory

The enrichment or depletion of isotopes in a substance is mainly controlled by mass induced difference in vibrational energies (Bigeleisen and Mayer, 1947; Urey, 1947). The details of this theory has been reiterated in many reviews (Richet et al., 1977; Kieffer, 1982; Oneil, 1986; Chacko et al., 2001; Schauble, 2004; Liu Q. et al., 2010; Young et al., 2015; Dauphas and Schauble, 2016; Blanchard et al., 2017). Generally, the equilibrium isotope fractionation factor (α) between substances A and B can be expressed as

$$\alpha_{A-B} = \frac{\beta_A}{\beta_B} \tag{1}$$

where the β factors are the reduced partition function ratios and can be calculated by (assuming only one atom in a compound is substituted):

$$\beta = \prod_i^N \frac{u_i^* \exp\left(-\frac{u_i^*}{2}\right)[1 - \exp(-u_i)]}{u_i \exp\left(-\frac{u_i}{2}\right)[1 - \exp(-u_i^*)]} \tag{2}$$

where

$$u_i = \frac{h\nu_i}{kT} \tag{3}$$

Here, ν_i represents the ith harmonic vibrational frequency. h is the Planck's constant and k is the Boltzmann's constant and T is the temperature in Kelvin. N is the number of harmonic vibrational modes. For a molecule with n atoms, N equals to 3n-5 for linear molecules or 3n-6 for non-linear polyatomic ones. The superscript "*" refers to the heavy isotope substituted molecules and the one without superscript is with the light isotope.

For crystals, the β factor can be calculated by

$$\beta = \left[\prod_i^N \prod_{\{q\}} \frac{u_{q,i}^*}{u_{q,i}} \frac{\exp\left(-\frac{u_{q,i}^*}{2}\right)[1 - exp(-u_{q,i})]}{\exp\left(-\frac{u_{q,i}}{2}\right)[1 - exp(-u_{q,i}^*)]} \right]^{1/N_q} \tag{4}$$

where the second product is performed on a uniform grid of N_q q-vectors in the Brillouin zone.

The fractionation between two substances is often expressed in the term of $1000 \cdot \ln(\alpha) = 1000 \cdot \ln(\beta_A) - 1000 \cdot \ln(\beta_B)$. Thus, one can easily obtain isotope fractionation via computation of frequencies related to isotopically different substances.

2.2. Selection of theoretical levels and basis sets

For quantum chemistry based frequency calculation, both theoretical methods (HF, DFT, MP2, CCSD, etc.) and basis sets can directly affect the final results. To choose the proper theoretical level and basis set, the β factors of $Mg(H_2O)_6^{2+}$ and brucite are investigated (Table 1). Rustad et al. (2010) suggested that the hybrid functional B3LYP method (Becke, 1993; Lee et al., 1988) combined with 6-311 + + G(2d,2p) basis set could produce reliable harmonic frequencies for solids and solutions. Thus, we have specifically tested the B3LYP hybrid functional method. The MP2 method (Head-Gordon et al., 1988) is also tested because of its better treatment on dispersion interactions and hydrogen bonding (Xantheas, 1995). To include the long-range solvation effects, the implicit solvent PCM model (e.g., Tomasi et al., 2005) has been also checked.

Table 1
Calculated β factors (^{26}Mg/^{24}Mg) of $Mg(H_2O)_6^{2+}$ and brucite (55-atom model) at 25 °C under different theoretical levels.

$Mg(H_2O)_6^{2+}$	β
B3LYP/6-31G*	1.02594 (1.02657)[a]
B3LYP/6-311G*	1.02724 (1.02747)[a]
B3LYP/6-311 + + G(2d,2p)	1.02437 (1.02424)[a]
B3LYP/aug-cc-pVDZ	1.02419 (1.02312)[a]
B3LYP/aug-cc-pVTZ	1.02421 (1.02415)[a]
MP2/6-311 + + G(2d,2p)	1.02510
MP2/aug-cc-pVDZ	1.02484
Brucite (55 atoms)[b]	β
B3LYP/6-31G*	1.02721
B3LYP/6-311G*	1.02889
B3LYP/6-311 + + G(2d,2p)	1.02652

[a] Results in the brackets are carried out with the explicit-plus-implicit solvent model.

[b] During calculations of β, no atoms are fixed, because the 55-atom-cluster are too small.

Table 2
Descriptions of model clusters of minerals and aqueous species.

Minerals	Total atoms[a]	Mg−O bond length (Å)[b]	Minerals	Total atoms[a]	Mg−O bond length (Å)[b]
Magnesite	111(25)	2.112(2.113)	Dolomite	111(25)	2.093(2.091)
Calcite	165(25)	2.163(2.168)	Aragonite	157(25)	2.434(2.467)
Brucite	127(31)	2.110(2.110)	Diopside	100(18)	2.097
Forsterite (M1)	99(19)	2.110	Enstatite (M1)	104(18)	2.102
Forsterite (M2)	106(22)	2.158	Enstatite (M2)	74(17)	2.163
Spinel	169(17)	1.973	Tremolite (M1)	97(19)	2.103
Tremolite (M2)	98(18)	2.108	Tremolite (M3)	99(19)	2.099

Aqueous species	Mg−O bond length (Å)[b]	Aqueous species	Mg−O bond length (Å)[b]
$Mg(H_2O)_{30}^{2+}$	2.116(2.120)	$Mg(H_2O)_{36}^{2+}$	2.117(2.118)
$MgHCO_3(H_2O)_{30}^{+}$	(2.059)	$MgHCO_3(H_2O)_{36}^{+}$	(2.057)
$MgOH(H_2O)_{30}^{+}$	(2.118)	$MgOH(H_2O)_{36}^{+}$	(2.113)

[a] "Total atoms" refers to the number of atoms used in the modeling. The atom numbers in brackets are those in the flexible part used in frequency calculations. For calcite and aragonite, since Mg occurs as a trace element, relatively larger clusters are used.

[b] Mg−O bond lengths are shown as mean values. All of the corresponding Mg−O bond lengths are listed in Table S8. For aqueous species, the Mg−O bond lengths are the average of all four conformers. The data out of brackets are calculated at B3LYP/6-31G*, in the brackets are calculated at B3LYP/6-311G* level.

The B3LYP methods with 6-311 + +G(2d,2p), aug-cc-pVDZ and aug-cc-pVTZ basis sets generate very similar β factors for $Mg(H_2O)_6^{2+}$ (Table 1), suggesting a converged value has been achieved at ~1.0242. However, the β factors of B3LYP methods with 6-31G* and 6-311G* basis sets are 1‰ - 3‰ larger. For the case of brucite, we found a similar trend, i.e., the results of 6-31G* and 6-311G* are larger than that of 6-311 + +G(2d,2p) by about 1‰–3‰. It indicates that β factors of minerals are also sensitive to basis sets. If we use the same theoretical level for both mineral and aqueous solution, most of the systematic errors will be canceled. For example, Mg isotope fractionations between brucite and $Mg(H_2O)_6^{2+}$ are 1.2‰, 1.6‰ and 2.1‰ at 6-31G*, 6-311G* and 6-311G + +(2d,2p) levels, respectively. The differences are within 1.0‰ even without any frequency scaling treatment. Considering the sizes of clusters involved in this study are all very large (often larger than 100 atoms, see Table 2), the theoretical levels employed are B3LYP/6-31G* and B3LYP/6-311G*.

To further check the reliability of frequency calculations, Mg−O vibrational frequencies of $Mg(H_2O)_6^{2+}$ are compared with previous theoretical and experimental results (Mink et al., 2003; Kapitán et al., 2010) (Table 3). Two vibrational modes, which are closely related to isotope substitution, are identified, i.e., antisymmetric stretching (double degeneracy) and symmetric stretching. The calculated frequencies are smaller than previous experimental results. The application of PCM model increases the frequencies by about 20 cm^{-1}. These are similar to what has been found in Schott et al. (2016). The frequencies calculated at B3LYP/6-31G* and B3LYP/6-311G* are close to those calculated at much higher theoretical levels. Therefore, no frequency scaling treatments are used for the cluster-model-based calculations, which are carried out with Gaussian09 D.01 software (Frisch et al., 2013).

2.3. The isotope fractionation calculation methods of minerals

2.3.1. Volume variable cluster model (VVCM)

Molecule-like clusters could be used to represent mineral

Table 3
The calculated Mg−O vibration frequencies (cm^{-1}, Raman active stretching modes) of $Mg(H_2O)_6^{2+}$ and those of previous experimental and theoretical results.[*]

	Antisymmetric	Symmetric
Previous study		
Exp[a]		355
Exp[b]	314	365
B3LYP/aug-cc-pVTZ[a]	246	318
B3LYP/6-311 + +G**[a]	249(263)	314(337)
This study		
B3LYP/6-31G*	258(276)	320(336)
B3LYP/6-311G*	262(280)	323(341)
B3LYP/6-311 + +G(2d,2p)	249(266)	317(336)
B3LYP/aug-cc-pVDZ	246(260)	312(322)
B3LYP/aug-cc-pVTZ	248(266)	318(337)

[*] The frequencies in brackets are calculated with the PCM solvent model.
[a] Theoretical and experimental frequencies of Kapitán et al. (2010).
[b] Experimental frequencies of Mink et al. (2003).

environments (Gibbs, 1982). The isotope effect is indeed a local effect and mostly affected by the next nearest neighborhood atoms (i.e., the NNN rule). With a cluster size larger than this requirement, the isotope effect of the interested atom can be properly addressed. Recently, by following the idea of Liu and Tossell (2005) and Rustad et al. (2010), we developed a modified cluster-model-based method named the volume-variable-cluster-model (VVCM) method (Liu, 2013; Li and Liu, 2015; He and Liu, 2015; He H. et al., 2016). This method can employ higher-level theoretical treatments for solids. A few difficult issues, such as H-bonding in minerals, weak interactions and anharmonic effects, etc., can be addressed by VVCM.

For VVCM, the X-ray or neutron diffraction crystal structures are taken as the original input structures (e.g., from the American Mineralogist Structure Database: http://rruff.geo.arizona.edu/AMS/amcsd.php). The clusters are built at sufficiently large sizes (Table 2) with the interested atom (Mg) at the center and anion atoms (e.g., oxygen atom) at the outermost cutting places (Fig. 1). Hundreds of virtual point charges are added at certain distances to the outermost anion atoms (Fig. 1a). These virtual charge points are employed to maintain the electronic neutrality of the whole cluster and to constrain the positions of those outermost anion atoms.

Unlike the embedded cluster method (Rustad et al., 2008, 2010), the VVCM method does a whole-cluster free optimization. By slightly adjusting the positions of point charges, i.e., the distances from the outermost anion atoms to the point charges, the cluster can be repeatedly optimized to the lowest energy point (Fig. S1). Once the structure of the lowest energy is found, vibrational frequencies are then calculated with a special fixation treatment of outer layers' atoms (Fig. 1b, Table 2), to let the calculated frequencies obey the Redlich-Teller product rule (Redlich, 1935) (See Supplementary material for the details of VVCM).

2.3.2. Periodic boundary methods

Currently, the periodic boundary and phonon-based method coupled with the first-principles density functional theory (DFT) calculation is a good choice for isotope fractionations between minerals (Meheut et al., 2007, 2009, 2010; Meheut and Schauble, 2014; Blanchard et al., 2009, 2015; Huang et al., 2013, 2014; Wu et al., 2015).

Here, for comparison, we have performed first-principles DFT calculations based on periodic boundary conditions to calculate the β factors of brucite, magnesite and dolomite. The calculations are carried out with VASP code (Kresse and Furthmüller, 1996). The Perdew, Burke and Ernzerhof (PBE) (Perdew et al., 1996) of generalized gradient approximation (GGA) is used. The pseudopotentials are extracted from VASP's library, i.e., Mg (s2p0), C (s2p2), O (s2p4), H (s1) and Ca
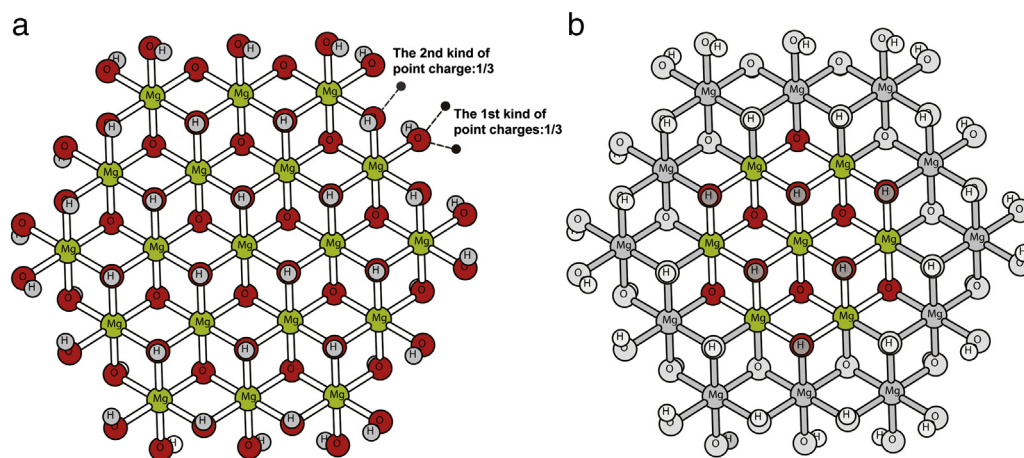
a

b

The 2nd kind of point charge:1/3

The 1st kind of point charges:1/3

nearest neighborhood (NNN) rule of the cluster size requirement.

Fig. 1. An illustration of mineral cluster model used in this study. (a) Brucite (127 atoms). The cluster is cut from experimentally determined brucite lattice. Two kinds of virtual point charges are used to maintain the electronic neutrality of the whole structure. Each of them is associated with a different type of surface oxygen atoms and with the same valence of 1/3. For a clear view, only 3 point charges are illustrated here. There are actually hundreds of point charges surrounding the surface of cluster model. (b) Brucite cluster for the computation of vibrational frequencies. The outer shell atoms (in grey) are fixed at the optimized positions. The inner flexible part has 31 atoms and obeys the next

(s2d0.01). The plane-wave energy cutoff is set as 600 eV and the Brillouin-zone integration is performed with the Monkhorst–Pack scheme using a $3 \times 3 \times 3$ k-mesh point. The unit-cell structural relaxation is converged if Hellmann-Feynman forces are smaller than 1e-4 eV/Å (Feynman, 1939).

The supercells are obtained from the optimized unit-cell by using PHONOPY code (Togo and Tanaka, 2015). $4 \times 4 \times 2$ supercell comprised of 160 atoms is used for brucite and $2 \times 2 \times 2$ supercells comprised of 80 atoms are used for magnesite and dolomite. The Hessian matrix is calculated with density functional perturbation theory (DFPT). The phonon frequencies are calculated at center of the Brillouin zone to allow comparisons with experimental Raman and infrared spectra. After tests, we finally use $2 \times 2 \times 2$ q mesh to generate frequencies for the β factor calculations.

2.3.3. The calculation method of amorphous calcium carbonates (ACCs)

Mg isotope fractionations between ACCs and aqueous Mg^{2+} are theoretically studied for the first time. The ACC complexes lack long-range order and their structures are still under debating (Fernandez-Martinez et al., 2017). Goodwin et al. (2010) performed reverse Monte Carlo modeling on Ca-ACC X-ray scattering data. The average Ca coordination numbers were obtained as 5.3 and 5.8 (± 1.5) for different modeling conditions. They found that the ACC structure consists of a nanoporous, cationic Ca-rich framework and a Ca-poor, carbonate/water rich interconnected channel network. However, Cobourne et al. (2014) found that the distribution of Ca in ACCs was homogeneous and there were no evidence for the presence of Ca-poor channels. Besides, Lin et al. (2015) suggested that there were 4–4.5 carbonate ions (CO_3^{2-}) surrounding each Mg^{2+}, and at least one water molecule was coordinated to each Mg^{2+} in Mg-ACC solids.

Because ACCs are amorphous materials instead of crystals, they can be simulated properly with large molecule-like clusters terminated by H atoms (Fig. 2). Based on the experimental observations, we build three local configurations of Mg-rich framework to represent Mg-ACCs. The first one is Mg^{2+} surrounded by four monodentate carbonate ions and two water molecules (Fig. 2a). The second one is Mg^{2+} surrounded by one bidentate carbonate ion, two monodentate carbonate ions and two water molecules (Fig. 2b). The third cluster is a five-coordinated Mg^{2+} surrounded by four monodentate carbonate ions and one water molecule (Fig. 2c). A magnesite-like cluster $Mg(CO_3)_6H_{12}^{2+}$ (Fig. 2d) is also simulated for comparison.

2.4. Solvation effects on Mg^{2+}-bearing aqueous species

2.4.1. Aqueous Mg^{2+}

Accurate estimation of solvation effects has long been a tremendous challenge in the isotope fractionation field (e.g., Oi and Yanase, 2001; Liu and Tossell, 2005; Li et al., 2009; Rustad and Dixon, 2009). The errors mostly arise from the uncertainty of local structure configurations, which is related to the weak interactions between solute and solvent molecules (i.e., short range effect), and electrostatic effects caused by polarized solvent molecules that lies in far distances (i.e., long range effect).

In our present work, we use an explicit-plus-implicit solvent method to include both short- and long-range effects. First, the "water-droplet" explicit solvent model is built, in which the solute is surrounded by a number of solvent molecules to simulate short range interactions (e.g., Liu and Tossell, 2005; Black et al., 2007; Li et al., 2009; Li and Liu, 2010, 2011; Fujii et al., 2011, 2013). For aqueous Mg^{2+} ion, Mg $(H_2O)_6^{2+}$ is proposed to be the first shell configuration by previous investigations (Palinkas et al., 1982; Ohtaki and Radnai, 1993; Markham et al., 2002). Initially, we build a starting cluster model of Mg $(H_2O)_6^{2+}$ by adding 6 water molecules around the Mg^{2+} ion and optimize its structure to reach a lowest energy point. Then we add another six-water-molecules to the second shell of this cluster model and optimize it again. By this way, step by step, we finally build a cluster model with 36 water molecules ($Mg(H_2O)_{36}^{2+}$). We repeat this procedure 4 times with different starting $Mg(H_2O)_6^{2+}$ structures to include the effect of different local configurations.

To evaluate the long range effects, the implicit solvent model is introduced. Polarizable continuum model (PCM) is the most popular solvent model which puts the solute molecules into a molecule-sized electrostatic cavity surrounded by dielectric medium to represent solvent environment (e.g., Tomasi et al., 2005). Rustad et al. (2010) used a single cluster ($Mg(H_2O)_{18}^{2+}$) and embedded it in continuum solvent model with COSMO (Klamt and Schuurmann, 1993) to simulate aqueous environment. In present work, we use much larger clusters combined with the PCM model to include both long- and short-range solvation effects.

2.4.2. $MgHCO_3^+$ and $MgOH^+$ aqueous species

It has been demonstrated that the inclusion of different Mg^{2+} species into the isotope fractionation estimation of bulk solution is important (Schott et al., 2016). Here, the β values of $MgHCO_3^+$ and $MgOH^+$ aqueous species are also calculated. These two species likely play an important role and their β factors are quite different from that of aqueous Mg^{2+} (Schott et al., 2016). The first coordination shells of $MgHCO_3^+$ and $MgOH^+$ were determined as $MgHCO_3(H_2O)_4^+$ and $MgOH(H_2O)_5^+$, respectively (Di Tommaso and de Leeuw, 2010a, 2010b; Schott et al., 2016; Stefánsson et al., 2017). The "explicit-plus-implicit" solvent model is used for them and the biggest clusters are with 36 water molecules (i.e., $MgHCO_3(H_2O)_{36}^+$ and $MgOH(H_2O)_{36}^+$).
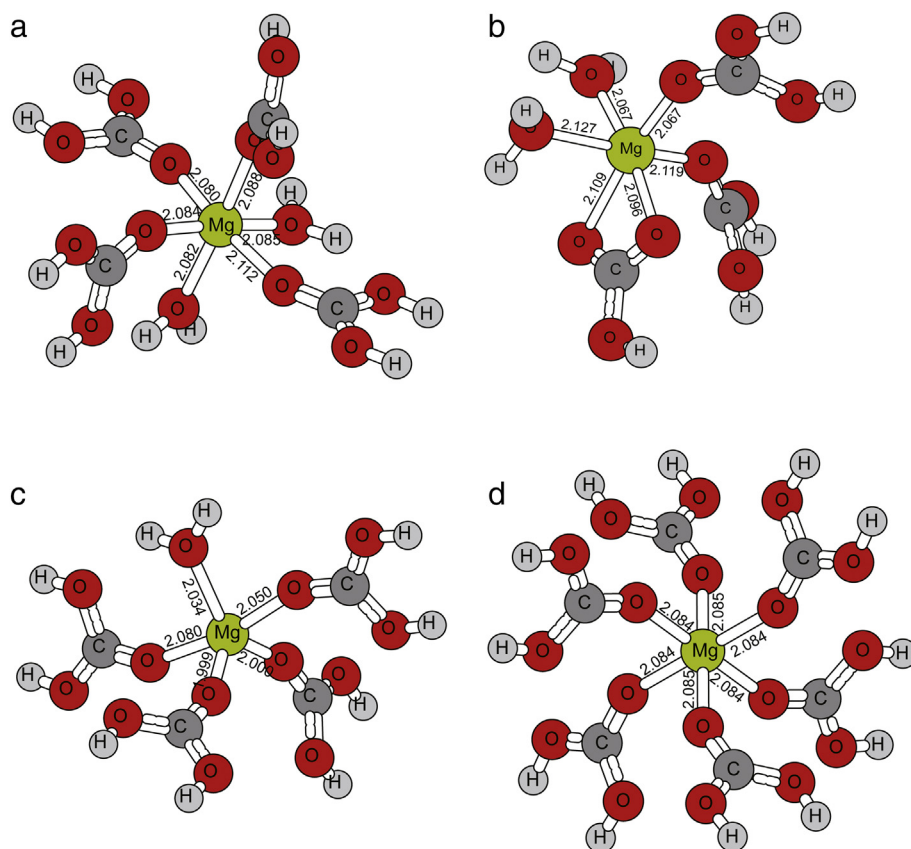
Fig. 2. Representative local configurations of ACCs and a magnesite-like cluster. (a) Six-coordinated monodentate $(H_2O)_2Mg(CO_3)_4H_8^{2+}$; (b) Six-coordinated bidentate $(H_2O)_2Mg(CO_3)_3H_5^{1+}$; (c) Five-coordinated $(H_2O)Mg(CO_3)_4H_8^{2+}$; (d) A magnesite-like cluster. The optimized Mg−O bond lengths are also shown.

2.5. The size effects

First, when using a cluster-based method to study minerals, the size of cluster can influence the β factors. Here, β factors of two brucite clusters with different sizes (55 atoms and 127 atoms) are calculated at B3LYP/6-31G* level to test the size effect. The difference is about 0.6‰ at room temperature, which indicates that the size effect may cause small errors on the β factors. Consequently, the clusters used here are all sufficiently large (Table 2).

Second, the size effect of periodic boundary method is also important. The β factors of brucite with the unit-cell (5 atoms) and a $2 \times 2 \times 2$ (40 atoms) supercell are calculated at room temperature. The results are 1.02090 and 1.02519 respectively, indicating the need for using large supercells. The β factor calculated using $4 \times 4 \times 2$ (160 atoms) supercell equals 1.02536, which is close to 1.02519, suggesting the convergence is reached. Based on these tests, supercells with sufficient sizes are used in this study.

3. Results

3.1. β factors

3.1.1. Mg^{2+}-bearing aqueous species

The solvation effects of aqueous Mg^{2+} ion are evaluated by the water droplet method (i.e., explicit solvent model) and the explicit-plus-implicit solvent model, respectively. The results of the water droplet method are listed in Table S2. With increasing water molecules in the clusters, the β factors generally converge to a certain value (no more size effect). Similar trends are found in the results of the explicit-plus-implicit solvent model for aqueous Mg^{2+}, $MgHCO_3^+$ and $MgOH^+$ species (Table 4, Tables S3, S4). The preferred value is chosen as the average value of several "converged" clusters. Large standard deviations are observed, indicating local configurations have a significant

Table 4
The calculated β factors ($^{26}Mg/^{24}Mg$) of aqueous Mg^{2+} ion by the explicit-plus-implicit solvent model at 25 °C*.

Cluster	6-31G*	6-311G*	Cluster	6-31G*	6-311G*
$Mg(H_2O)_6^{2+}$_A	1.02700	1.02673	$Mg(H_2O)_{24}^{2+}$_A	1.02429	1.02510
$Mg(H_2O)_6^{2+}$_B	1.02628	1.02699	$Mg(H_2O)_{24}^{2+}$_B	1.02301	1.02600
$Mg(H_2O)_6^{2+}$_C	1.02607	1.02813	$Mg(H_2O)_{24}^{2+}$_C	1.02472	1.02487
$Mg(H_2O)_6^{2+}$_D	1.02695	1.02803	$Mg(H_2O)_{24}^{2+}$_D	1.02485	1.02415
Average	**1.02657**	**1.02747**	**Average**	**1.02422**	**1.02503**
$Mg(H_2O)_{12}^{2+}$_A	1.02569	1.02787	$Mg(H_2O)_{30}^{2+}$_A	1.02596	1.02608
$Mg(H_2O)_{12}^{2+}$_B	1.02625	1.02698	$Mg(H_2O)_{30}^{2+}$_B	1.02465	1.02633
$Mg(H_2O)_{12}^{2+}$_C	1.02603	1.02698	$Mg(H_2O)_{30}^{2+}$_C	1.02532	1.02521
$Mg(H_2O)_{12}^{2+}$_D	1.02590	1.02781	$Mg(H_2O)_{30}^{2+}$_D	1.02530	1.02495
Average	**1.02597**	**1.02741**	**Average**	**1.02531**	**1.02564**
$Mg(H_2O)_{18}^{2+}$_A	1.02433	1.02436	$Mg(H_2O)_{36}^{2+}$_A	1.02573	1.02558
$Mg(H_2O)_{18}^{2+}$_B	1.02376	1.02499	$Mg(H_2O)_{36}^{2+}$_B	1.02516	1.02542
$Mg(H_2O)_{18}^{2+}$_C	1.02395	1.02558	$Mg(H_2O)_{36}^{2+}$_C	1.02502	1.02625
$Mg(H_2O)_{18}^{2+}$_D	1.02373	1.02448	$Mg(H_2O)_{36}^{2+}$_D	1.02559	1.02558
Average	**1.02394**	**1.02485**	**Average**	**1.02537**	**1.02571**
			Preferred value[a]	**1.02534**	**1.02568**
			σ	4.2e-04	5.0e-04

* The "Average" data in bold are the mean values of 4 clusters (i.e., cluster A, B, C, D).

[a] The "preferred value" are the average results of 8 clusters ($4 \times Mg(H_2O)_{30}^{2+}$ and $4 \times Mg(H_2O)_{36}^{2+}$).

influence on β factors. Therefore, it is necessary to sample different local configurations of aqueous species.

Table 5 shows the polynomial fit parameters of $1000\ln(\beta)$ vs. $10^6/T^2$ for minerals and solutions. The calculated β factors of Mg^{2+}-bearing aqueous species follow the order of $MgHCO_3^+_{(aq)} > MgOH^+_{(aq)} > Mg^{2+}_{(aq)}$, which is consistent with what was found in Schott et al. (2016). The average Mg−O bond lengths of these species show the opposite trend (Table 2, Table S8). However, the absolute

Table 5

Polynomial fit parameters of calculated (^{26}Mg/^{24}Mg) β factors as the form of $1000 \cdot \ln(\beta_{26-24}) = ax + bx^2 + cx^3$, in which $x = 10^6/T^2$ and T is the temperature in Kelvin (273–1273 K).[*]

	a	b	c
Mg$_{(aq)}$	2.4205	-2.1133×10^{-2}	3.2587×10^{-4}
Mg$_{(aq)}$[a]	2.4534	-2.1460×10^{-2}	3.2524×10^{-4}
MgOH$^+$[a]	2.5293	-2.2416×10^{-2}	3.2675×10^{-4}
MgHCO$_3^+$[a]	2.6977	-2.4298×10^{-2}	3.2457×10^{-4}
Magnesite	2.2434	-1.3933×10^{-2}	1.8177×10^{-4}
Magnesite[a]	2.3495	-1.5199×10^{-2}	1.9873×10^{-4}
Magnesite[b]	2.0458	-1.2673×10^{-2}	1.7655×10^{-4}
Dolomite	2.3650	-1.4858×10^{-2}	1.8454×10^{-4}
Dolomite[a]	2.4028	-1.5339×10^{-2}	1.9208×10^{-4}
Dolomite[b]	2.1459	-1.3020×10^{-2}	1.6920×10^{-4}
Calcite	1.7303	-9.4774×10^{-3}	1.4119×10^{-4}
Calcite[a]	1.7377	-9.7094×10^{-3}	1.4682×10^{-4}
Aragonite	1.0535	-6.3866×10^{-3}	1.3051×10^{-4}
Aragonite[a]	1.1639	-6.7848×10^{-3}	1.2916×10^{-4}
Brucite	2.6424	-1.8344×10^{-2}	1.7339×10^{-4}
Brucite[a]	2.7011	-1.9274×10^{-2}	1.8888×10^{-4}
Brucite[b]	2.4652	-1.6712×10^{-2}	1.7178×10^{-4}
(H$_2$O)$_2$Mg(CO$_3$)$_4$H$_8^{2+}$[a]	2.4605	-1.7572×10^{-2}	1.9939×10^{-4}
(H$_2$O)$_2$Mg(CO$_3$)$_3$H$_5^{1+}$[a]	2.6442	-2.1377×10^{-2}	2.6944×10^{-4}
(H$_2$O)Mg(CO$_3$)$_4$H$_8^{2+}$[a]	2.6113	-1.9570×10^{-2}	2.2917×10^{-4}
Forsterite	2.3870	-1.5128×10^{-2}	1.4897×10^{-4}
Diopside	2.5287	-1.4671×10^{-2}	1.2343×10^{-4}
Enstatite	2.5292	-1.7087×10^{-2}	1.6996×10^{-4}
Spinel	3.1996	-2.6238×10^{-2}	2.9206×10^{-4}
Tremolite	2.5503	-1.5652×10^{-2}	1.3901×10^{-4}

[*] The results without special description are calculated at B3LYP/6-31G* level.

[a] The results are calculated at B3LYP/6-311G* level.

[b] The results of PBE calculations.

fractionation magnitudes between ours and those of Schott et al. (2016) are different. For example, our calculated fractionation between MgHCO$_3^+$$_{(aq)}$ and Mg^{2+}$_{(aq)}$ is smaller than their value by ~1.6‰ at room temperature. This difference is probably caused by different sizes of clusters we used. They followed the method of Fujii et al. (2011) and Fujii et al. (2013) to use quite small clusters, which consist of only the first hydration shell of Mg^{2+}. One of the consequences is that H atoms will form H-bonding with the neighborhood oxygen atoms in the same coordination shell instead of with those at the second shell. For example, the small MgHCO$_3$(H$_2$O)$_4^+$ cluster will form H-bondings and become a "triple-ion-structure" (OH-Mg-H$_2$CO$_3$(H$_2$O)$_3^+$), which is likely an artificial structure and may have significant effects on its β factor. If with more water molecules added at the second coordination shell, this "triple-ion-structure" won't be formed.

3.1.2. Carbonate minerals and brucite

Table 6 shows the calculated β factors of carbonate minerals and brucite. Relative to aqueous Mg^{2+} ion, carbonates enrich light Mg isotopes. Aragonite has the lowest β factor among the studied carbonate minerals. It is because Mg^{2+} substitutes Ca^{2+} into a 9-coordinated

Table 6

The calculated β factors (^{26}Mg/^{24}Mg) of carbonate minerals, brucite, three ACC representative clusters and a magnesite-like cluster (25 °C).

Minerals	B3LYP/6-31G*	B3LYP/6-311G*	PBE
Magnesite	1.02402	1.02510	1.02190
Calcite	1.01864	1.01870	
Dolomite	1.02530	1.02569	1.02300
Aragonite	1.01130	1.01250	
Brucite	1.02804	1.02862	1.02620
ACC_(H$_2$O)$_2$Mg(CO$_3$)$_4$H$_8^{2+}$		1.02608	
ACC_(H$_2$O)$_2$Mg(CO$_3$)$_3$H$_5^{1+}$		1.02781	
ACC_(H$_2$O)Mg(CO$_3$)$_4$H$_8^{2+}$		1.02760	
Mg(CO$_3$)$_6$H$_{12}^{2+}$		1.02477	

lattice site and generates weaker Mg−O bonds (Table 2, Table S8). A previous experimental study showed that aragonite was enriched with heavy Mg isotopes relative to magnesite or even dolomite (Wang et al., 2013), which was supported by the evidence of short Mg−O bond length (~2.08 Å) of aragonite reported in Finch and Allison (2007). However, Finch and Allison (2007) actually didn't confirm whether the Mg atom was accommodated in aragonite structure or in the nano-domains of unknown phases. For brucite, our results show that brucite enriches heavy Mg isotopes relative to coexisting aqueous Mg^{2+} (Table 6, Fig. 3a).

3.1.3. ACCs

The calculated β factors of three ACC representative clusters (i.e., ((H$_2$O)$_2$Mg(CO$_3$)$_4$H$_8^{2+}$, (H$_2$O)$_2$Mg(CO$_3$)$_3$H$_5^{1+}$ and (H$_2$O)Mg(CO$_3$)$_4$H$_8^{2+}$) and a magnesite-like cluster (i.e., Mg(CO$_3$)$_6$H$_{12}^{2+}$) are listed in Table 6. The calculated β factor of Mg(CO$_3$)$_6$H$_{12}^{2+}$ is slightly smaller than that of magnesite (calculated by VVCM) by ~0.3‰ (i.e., 1.02477 vs. 1.02510). The ACCs have larger β factors than aqueous Mg^{2+} and carbonates minerals. Overall, the β factors generally follow the order of brucite > ACCs > dolomite > magnesite > calcite > aragonite (Table 6, Fig. 3a).

3.1.4. PBE calculation results

A frequency scale factor is often used to correct the errors in PBE calculations, because PBE functional generally lead to the over-estimation of structure parameters and underestimation of vibrational frequencies (e.g., Meheut et al., 2009; Schauble et al., 2006; Schauble, 2011). The optimized structure parameters are compared with measurements (Ross and Reeder, 1992; Chakoumakos et al., 1997; Ross, 1997) and previous first principle studies (Meheut et al., 2010; Schauble, 2011) in Table S5. For all the structures, PBE calculations generally lead to a systematic overestimation of lattice parameters by 1–2%. The calculated vibrational frequencies at center of the Brillouin zone are compared with measurements in Fig. 4 and Table S6 (Hellwege et al., 1970; Dawson et al., 1973; Rutt and Nicola, 1974; Nicola et al., 1976; Pilati et al., 1998). Generally, the calculated frequencies are smaller than measured ones by ~5%. On the other hand, two O−H related modes of brucite show larger vibrational frequencies than measured ones (by ~2%), which may be caused by anharmonicity. Here, we follow the procedure of Meheut et al. (2009) and consider the best linear fit of measured and calculated frequencies. The scale factor is obtained as 1.039 ± 0.005.

3.2. Mg isotope fractionations between minerals and solutions

For the case of magnesite vs. aqueous Mg^{2+}, the calculated Mg isotope fractionations are in good agreement with previous theoretical studies (Rustad et al., 2010; Pinilla et al., 2015) (Fig. 5a), and slightly smaller than the experimental data (Pearce et al., 2012).

For dolomite vs. aqueous Mg^{2+}, although our results are in excellent agreement with a previous theoretical study (Pinilla et al., 2015) (Fig. 5b), but the experimental measurements (Li et al., 2015) suggested larger fractionations (i.e., −0.93‰ at 130 °C, −0.85‰ at 160 °C and −0.65‰ at 220 °C). Larger fractionations (i.e., −2.0‰ to −2.7‰) between dolomite and coexisting solutions were also reported by other studies (Higgins and Schrag, 2010; Fantle and Higgins, 2014). However, a field observation of Geske et al. (2015) suggested that this fractionation was in the range of −0.7‰ to +0.1‰, which is close to our results.

For calcite vs. aqueous Mg^{2+}, the calculated fractionations are −6.6‰ and −6.8‰ at 298 K for 6-31G* and 6-311G* levels, respectively (Fig. 5c). Our results again are in excellent agreement with Pinilla et al. (2015) (−6.7‰). However, several experimental studies (Immenhauser et al., 2010; Li et al., 2012; Saulnier et al., 2012; Mavromatis et al., 2013) reported significantly smaller isotope fractionations between calcite and aqueous Mg^{2+} (from −1.7‰ to
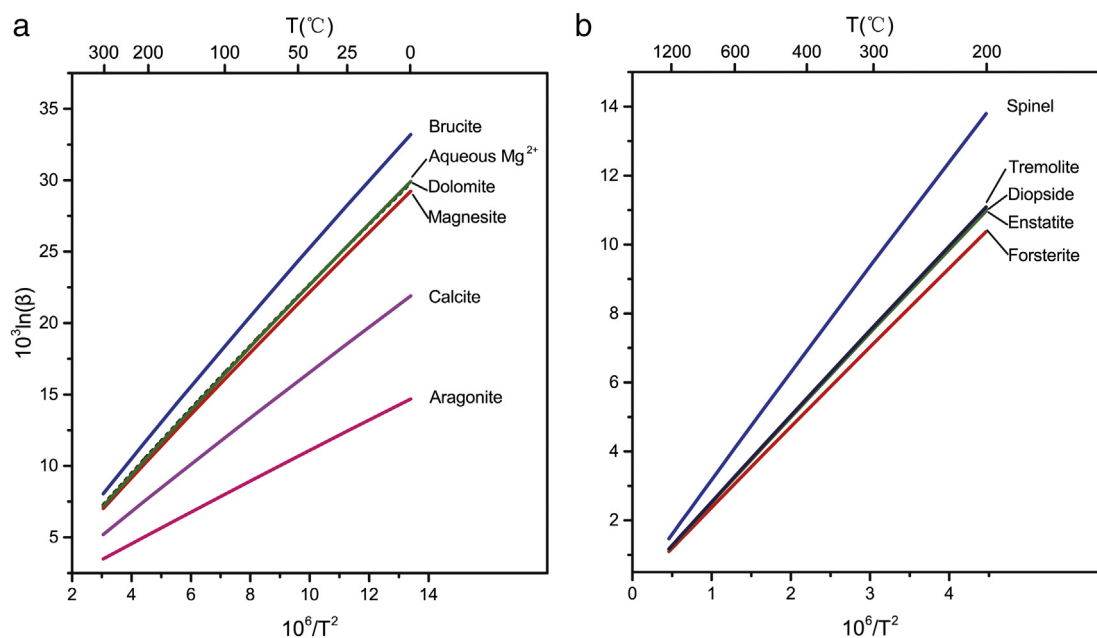
Fig. 3. Temperature dependence of $1000 \cdot \ln(\beta_{26-24})$ for minerals and aqueous Mg^{2+}. (a) Carbonate minerals, brucite and aqueous Mg^{2+} (at B3LYP/6-311G*). (b) High-temperature minerals (at B3LYP/6-31G*).

− 3.5‰).

For aragonite vs. aqueous Mg^{2+}, the calculated fractionations are larger than − 10‰ at room temperature and are significantly different from the experimental results (Wang et al., 2013), which suggested much smaller Mg isotope fractionations (~ − 1.1‰) (Fig. 5d).

For brucite vs. aqueous Mg^{2+}, the fractionations at 25 °C are predicted as + 2.7‰ and + 2.9‰ at B3LYP/6-31G* and B3LYP/6-311G* levels, respectively (Fig. 5e), which are close to the values (about + 3.3‰ at PBE0/aug-cc-pVTZ(O,H,Mg)/cc-pVDZ(2nd Shell) level) reported in Colla et al. (2018). However, the predicted fractionations are larger than the results of previous brucite synthesis experiment (Wimpenny et al., 2014) by ~1.5‰ at 80 °C, and in contrast with another experimental observations (Li et al., 2014).

3.3. Mg isotope fractionations among minerals

There are fewer disagreements about isotope fractionations for the cases of mineral vs. mineral. Fig. 6 shows that, for brucite vs. dolomite, the results of VVCM and PBE methods are generally close to each other. For magnesite vs. dolomite, the calculated fractionations are: − 0.57‰ (B3LYP/6-311G*), − 1.25‰ (B3LYP/6-31G*), − 1.07‰ (PBE) at room temperature which are in good agreements with those of Schauble (2011) and Pinilla et al. (2015). The observed difference (~0.5‰) between B3LYP/6-31G* and B3LYP/6-311G* results is possibly related to different basis sets. There are also ~0.5‰ deviations between the three different PBE calculations. Note that both this study and Schauble (2011) used scaled frequencies to generate β factors. However, Pinilla et al. (2015) used the raw frequencies, but they fixed the lattice parameters as experimental values during structure relaxations. Meanwhile, Rustad et al. (2010) suggested the largest fractionation (− 2.24‰) for this case.

4. Discussion

4.1. Magnesite or dolomite vs. aqueous Mg^{2+} ion

There are small disagreements of Mg isotope fractionations between our calculations and previous experiments for magnesite or dolomite against aqueous Mg^{2+} ion (Fig. 5a–b). These disagreements are most likely caused by the existence of Mg^{2+}-bearing aqueous species other than aqueous Mg^{2+} ion (e.g., $MgHCO_3^+$, $MgCO_3^0$ and $MgOH^+$) in experimental solutions (Schott et al., 2016). Because these species have β factors larger than that of aqueous Mg^{2+}, the weighted total β factor of solution will be much larger than β factor of aqueous Mg^{2+}. Consequently, the experimentally measured Mg isotope fractionations (e.g., $\Delta^{26}Mg_{mag-solution}$) will be different from the calculated one (i.e., $\Delta^{26}Mg_{mag-Mg^{2+}(aq)}$), which uses aqueous Mg^{2+} to represent the solutions (Fig. 5a). The "calibrated results" in Fig. 5a are taken from the column of "Calibrated $\Delta^{26}Mg_{mag-Mg^{2+}_{(aq)}}$ (This study)" in Table S7. They are "calibrated" experimental results by excluding the contributions of $MgHCO_3^+$ and $MgOH^+$ species. They are obviously closer to our calculation results.

For dolomite vs. aqueous Mg^{2+} ion, the discrepancies may also be caused by the occurrence of other Mg^{2+}-bearing species in the experimental solutions. The experiments (Li et al., 2015) are conducted in concentrated electrolyte solutions at hydrothermal temperatures. Such conditions are found to increase the possibility of $Mg - SO_4^{2-}$ and $K^+ - Cl^-$ ion pairs (Akilan et al., 2006; He M. et al., 2016), which may also increase the chance of the $Mg - CO_3^{2-}$ and $Mg - HCO_3^{1-}$ ion pairs. Unfortunately, we are unable to quantify these effects due to unknown proportions of these aqueous Mg-bearing species.

4.2. Calcite or aragonite vs. aqueous Mg^{2+}

Large discrepancies exist in theoretical and experimental results of calcite or aragonite vs. aqueous Mg^{2+}. There are several reasons for them. First, Mg isotope compositions of carbonates could be strongly influenced by formation temperature, Mg/Ca ratio, precipitation rate and saturation state of solution (Saenger and Wang, 2014). For those experiments conducted at relatively low Mg/Ca ratios and low saturation states (Immenhauser et al., 2010; Mavromatis et al., 2013), Mg isotope fractionations might be affected by the precipitation rates of minerals and the dehydration rates of Mg^{2+}. Because of its high dehydration free energy (Di Tommaso and de Leeuw, 2010a, 2010b), when the rate of mineral precipitation is larger than the rate of Mg^{2+} ion dehydration, hydrated Mg^{2+} might be directly incorporated into the structure of minerals, which would possibly reduce the observed fractionations (Saenger and Wang, 2014). Second, the presence of
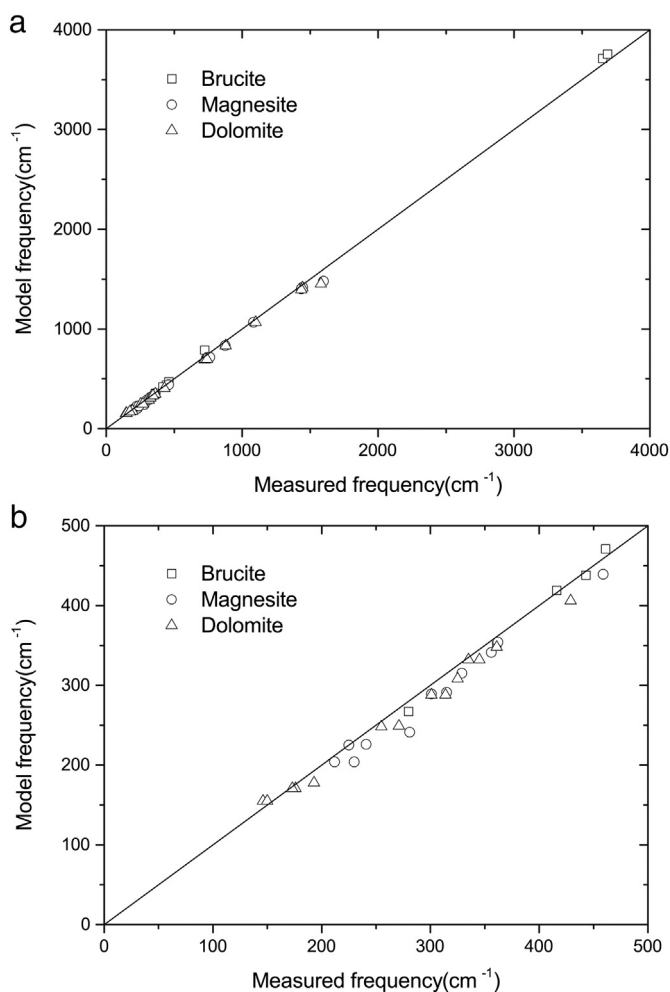
Fig. 4. Calculated vibrational frequencies (Raman and infrared) of PBE calculations compared with measurements. (a) all the vibrational modes; (b) modes with frequencies range from 0 to 500 cm^{-1}, which is closely related to Mg isotope substitution (Rustad et al., 2010; Schauble, 2011). The solid lines represent the 1:1 correlation. The experimental frequencies are taken from Dawson et al. (1973) for brucite, Hellwege et al. (1970) and Nicola et al. (1976) for dolomite, and Rutt and Nicola (1974) for magnesite.

intermediate phases, i.e., amorphous calcium carbonates (ACCs), serve as precursors to carbonate minerals (Clarkson et al., 1992; Wang et al., 2012). The effects of the presence of ACCs on Mg isotope fractionation are poorly understood. Third, magnesium occurs as a trace element in calcite and aragonite and their β factors are sensitive to Mg/Ca ratios in the structure, so-called as "the concentration effect" (Wang et al., 2017). In this study, there is only one Mg^{2+} substituted into the calcite and aragonite clusters, which conceptually corresponds to the dilute limit in Wang et al. (2017). However, the experiments were done at different Mg concentrations and probably were affected by the concentration effect.

For aragonite vs. aqueous Mg^{2+}, obvious discrepancies exist in theoretical predictions of this study and Pinilla et al. (2015) (Fig. 5d). It is hard to explain this deviation because in most of cases these two methods produce very close results. Pinilla et al. (2015) found that when Mg^{2+} substitutes Ca^{2+} into aragonite's lattice, a strong structure distortion would happen. The same phenomenon is also found in present work. For example, at B3LYP/6-311G* level, the optimized aragonite structure shows six Mg−O bonds ranging from 2.19 to 2.35 Å but with another three Mg−O bonds larger than 2.80 Å. Based on Mg−O bond lengths listed in Table S8, it is likely that the deviations are arise from the different local stable distorted structures used in these two

studies. Even it is in crystal, there are probably different stable configurations for a distorted local structure. Pinilla et al. (2015) and present work have possibly searched out different local stable configurations, which finally lead to different Mg isotope fractionations. The structural distortion may also be responsible for the small deviation between the results calculated at B3LYP/6-31G* and B3LYP/6-311G*.

4.3. The effect of ACCs on Mg isotope fractionations

At ambient temperatures, carbonate minerals often precipitate from solutions via intermediate phases (e.g., ACCs). Recently, many studies have focused on the formation and transition mechanism of these precursors. Systematic description of these precursors could be found in several recent reviews (Cartwright et al., 2012; Demichelis et al., 2017; Fernandez-Martinez et al., 2017; Rodriguez-Blanco et al., 2017). Knowing the details of these amorphous phases may provide important clues for isotope fractionations during carbonate crystallization processes.

Schematic representation of non-classical crystallization pathways of carbonate minerals are shown in Fig. 7. These multistage pathways are very sensitive to starting pH, temperature, impurities (e.g., Mg^{2+}, SO$_4$$^{2-}$, organics) and Mg/Ca ratios in the solutions (Radha et al., 2012; Rodriguez-Blanco et al., 2012, 2017; Purgstaller et al., 2016, 2017). At the beginning of the reaction pathway, single ions (e.g., Ca^{2+}, CO$_3$$^{2+}$, HCO$_3$$^-$) will bond together via ionic interactions and form linear chains, branches and rings structures (Demichelis et al., 2011). These relatively stable structures are called prenucleation clusters (Gebauer et al., 2008; Pouget et al., 2009). Through the aggregation and dehydration of the clusters in solution (Raiteri and Gale, 2010; Singer et al., 2012), ACC solids precipitate rapidly. Therefore, the local structure information of prenucleation clusters may be preserved in the AAC solids (Wallace et al., 2013). At near neutral starting pH, ACCs directly transform to calcite via dehydration and dissolution-reprecipitation mechanisms (Fig. 7, path 1) (Bots et al., 2012; Rodriguez-Blanco et al., 2012). While at basic pH (< 11.5), ACCs will transform to calcite via a vaterite intermediate (Fig. 7, path 2) (Rodriguez-Blanco et al., 2011, 2012, 2017). When temperatures are higher than 60 °C, ACCs will transform to aragonite via vaterite (Fig. 7, path 3) (Ogino et al., 1987).

The presence of Mg^{2+} will stabilize the ACC structures and promote the crystallization of Mg-calcite (Rodriguez-Blanco et al., 2012; Purgstaller et al., 2016), because Mg^{2+} have higher dehydration free energy compared to Ca^{2+} (Di Tommaso and de Leeuw, 2010a, 2010b). As Mg^{2+} content increases, higher temperatures are needed to provide the energy to dehydrate ACCs. This may explain why dolomite can only be precipitated at elevated temperatures (Rodriguez-Blanco et al., 2015).

There are only few works that have studied isotope compositions of carbonate precursors (ACCs) and their effects on the final isotope compositions of minerals. Gagnon et al. (2010) found that the formation of ACCs would weaken Ca isotope fractionation. Mavromatis et al. (2017) found that Mg isotope fractionations between ACCs and fluids were significantly smaller than the fractionation between calcite and fluid (i.e., −1.0‰ vs. −3.0‰ to −3.6‰). They therefore suggested that the isotope composition of ACCs was not preserved in the final calcite structure. The Mg isotope fractionation between ACCs and aqueous Mg^{2+} (0.0‰–2.0‰) has also been reported.

Equilibrium Mg isotope fractionations between ACCs and aqueous Mg^{2+} are theoretically studied here. All of the three representative clusters of ACCs have larger β factors than that of aqueous Mg^{2+} ion and carbonate minerals (Table 6). Goodwin et al. (2010) suggested that approximate 45% of Ca−O linkages in ACCs were bidentate. By using the weighted value of monodentate and bidentate β factors, and considering the offset (~0.3‰) between the β factors of Mg(CO$_3$)$_6$H$_{12}$$^{2+}$ and magnesite (111-atom VVCM model), a isotope fractionation of +1.45‰ is obtained between ACCs and aqueous Mg^{2+} at 25 °C, which falls into the range of experimental estimation (i.e., 0.0‰–2.0‰)
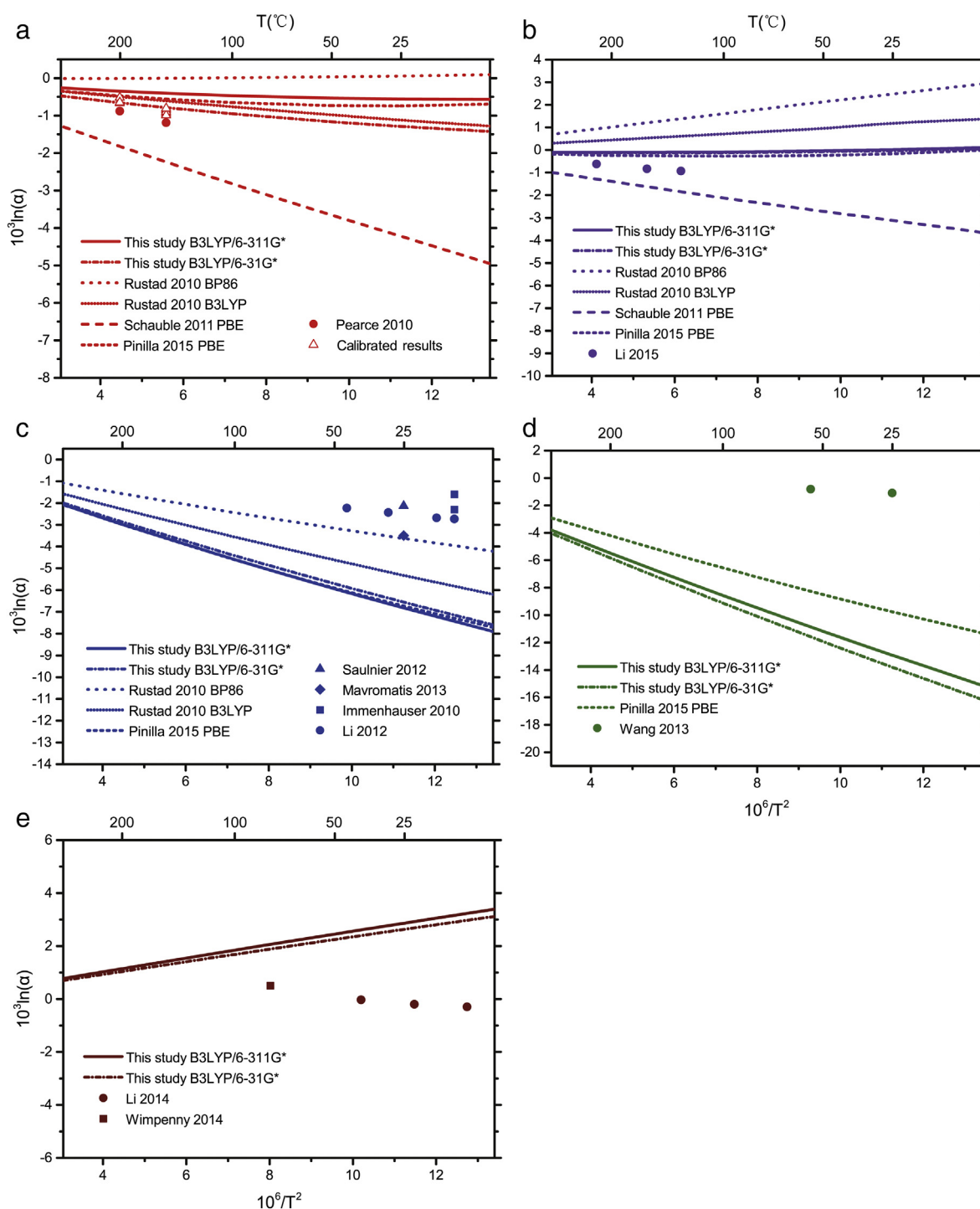
Fig. 5. Theoretical predictions of Mg isotope fractionations between minerals and aqueous Mg^{2+}. (a) Magnesite case. The open triangles represents the calibrated experimental results by excluding the effects of other Mg-bearing aqueous species (see Table S7) (Pearce et al., 2012; Schott et al., 2016); (b) Dolomite case. (c) Calcite case. (d) Aragonite case. (e) Brucite case. The results are calculated at B3LYP/6-31G* and B3LYP/6-311G* levels. The previous experimental (Immenhauser et al., 2010; Pearce et al., 2012; Saulnier et al., 2012; Li et al., 2012, 2014, 2015; Mavromatis et al., 2013; Wang et al., 2013; Wimpenny et al., 2014) and theoretical data (Rustad et al., 2010; Schauble, 2011; Pinilla et al., 2015) are shown for comparison.

(Mavromatis et al., 2017).

For calcite vs. solution, Mavromatis et al. (2017) reported the Mg isotope fractionation of −3.0‰ to −3.6‰. After excluding the effects of other Mg^{2+} aqueous species, this result is much smaller than our calculation value ($\sim$ −6.7‰). Nevertheless, in the experiment of Mavromatis et al. (2017), ACCs rapidly transformed to calcite within 25–60 min and was accompanied by a sharp increase of Mg content in the solids (see also Purgstaller et al., 2016) as well as a change of Mg

isotope fractionations from −1.0‰ to −3.0‰. Note that ACC-calcite transformation involved dissolution of ACCs and re-precipitation of calcite (Giuffre et al., 2015; Purgstaller et al., 2016). New calcite structures are formed from this supersaturation solution immediately. It is possible that this process may not be at chemical equilibrium.

Interestingly, after ACC-calcite transformation, the observed fractionation between solids and fluid became progressively more negative, i.e., from −3.1‰ to −3.6‰ (Mavromatis et al., 2017), which was
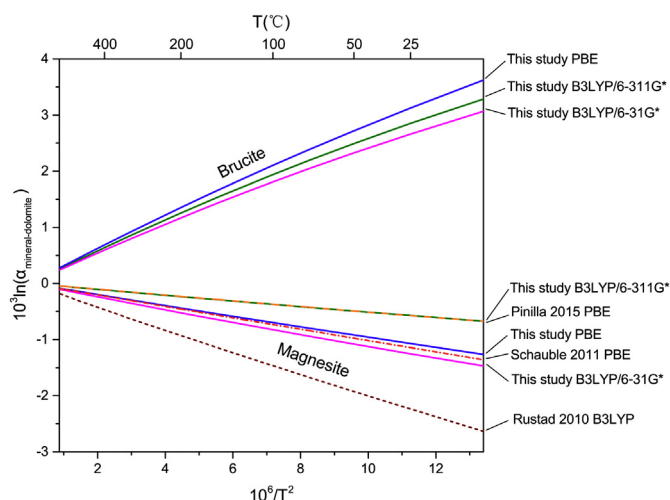
Fig. 6. Temperature dependence of $^{26}Mg/^{24}Mg$ fractionation factors for brucite and magnesite relative to dolomite. The results calculated with VVCM method are compared with those of PBE calculations. The fractionations reported by previous theoretical studies (Rustad et al., 2010; Schauble, 2011; Pinilla et al., 2015) are also shown here.

accompanied by progressive increasing of Mg content in the solids. Mavromatis et al. (2017) attributed this isotope shift to the increase of Mg content as reported in Pinilla et al. (2015). However, Wang et al. (2017) systematically studied the Mg concentration effect on cation substitutions and found the opposite trend, i.e., the Mg–O bonds become shorter as the increase of Mg in calcite. Obviously, further works are needed to reveal the mechanism of ACC-calcite precipitation and its effects on isotope fractionation, especially to determine whether it is an equilibrium process.

4.4. Brucite vs. aqueous Mg^{2+}

The origin of the discrepancies between our calculations and previous experiments for brucite vs. aqueous Mg^{2+} case is unclear. It is possible that the existence of Mg^{2+}-bearing complexes (e.g., $MgOH^+$) in experimental solutions lowers down the fractionation magnitude (Schott et al., 2016). However, Li et al. (2014) demonstrated that $MgOH^+$ accounted for only 0.1% of total Mg content in the solutions, that was not sufficient to cause the ~3‰ deviation.

It is possible that this discrepancy is caused by the approximations involved in our calculations. However, the predicted fractionations are close to the results of recent theoretical work (Colla et al., 2018). Colla et al. (2018) also found that the temperature dependencies reported in two previous experiment works (Wimpenny et al., 2014; Li et al., 2014)

can only be achieved by fixing the Mg–O bond lengths of aqueous Mg^{2+} to much smaller values (close to the Mg–O bond lengths of hydrated Mg^{2+} that are trapped in crystals). Besides, the $\Delta^{26}Mg_{brucite-dolomite}$ values from VVCM and PBE calculations are close to each other (Fig. 6, 2.9‰ vs. 3.1‰, at 25 °C). Fig. 5b shows that there is negligible fractionation between dolomite and aqueous Mg^{2+}, which are predicted by VVCM and PBE (Pinilla et al., 2015) calculations. That means both the VVCM and PBE methods also predict very similar $\Delta^{26}Mg_{brucite-Mg^{2+}_{(aq)}}$. Considering VVCM and PBE are based on completely different theoretical approaches, it is unlikely that the discrepancy is caused by the uncertainties of the calculations.

4.5. Applying VVCM to high-temperature phases

Previous studies of mantle minerals have observed measurable Mg isotope fractionations even at very high temperatures ($> 1000\,K$) (Wiechert and Halliday, 2007; Yang et al., 2009; Young et al., 2009; Liu et al., 2011; Pogge von Strandmann et al., 2011; Xiao et al., 2013), which were suggested to be serve as new geothermometers (Young et al., 2009). Investigation of Mg isotopes of mantle minerals is also important for the assessment of the Mg isotope composition of bulk silicate earth (BSE) and may provide information of planet formation processes (Young et al., 2015). Here, we extend VVCM calculations to high-temperature phases. The Mg isotope fractionations between fosterite, diopside, enstatite, spinel and tremolite are theoretically predicted.

The calculated β factors of high-temperature minerals are listed in Table 7 and plotted in Fig. 3b. For spinel, we only investigate the common condition that Mg atoms are at the tetrahedral sites and Al atoms occupy the octahedral sites. For those minerals possessing more than one Mg sites, the final β factors are the weighted average result of all Mg sites. The fractionations between pyroxenes and forsterite are predicted as $10^3 ln\alpha_{Di-Fo} \approx 10^3 ln\alpha_{En-Fo} = 0.12‰$ at 800 °C (Fig. 8), which are close to previous theoretical studies (Schauble, 2011; Huang et al., 2013) and natural sample observations (Wiechert and Halliday, 2007; Yang et al., 2009; Handler et al., 2009; Huang et al., 2011). Slightly bigger fractionations are found between tremolite and forsterite (e.g., ~0.14‰ at 800 °C). The calculated β factors are in the order of spinel > tremolite > diopside > enstatite > forsterite, which is consistent with previous first-principles studies (Huang et al., 2013; Schauble, 2011). Liu S. et al. (2010) carefully compared the bonding environments (Mg and O coordination) of amphibole, olivine and pyroxene, they also suggested similar Mg isotope enrichment order.

Significant inter-mineral fractionations are found between spinel and forsterite even at high temperatures (Fig. 8). The calculated fractionation is 0.70‰ at 800 °C, which is slightly smaller than the results of previous theoretical study by ~0.1‰ (Schauble, 2011). On the other hand, Macris et al. (2013) experimentally obtained similar value
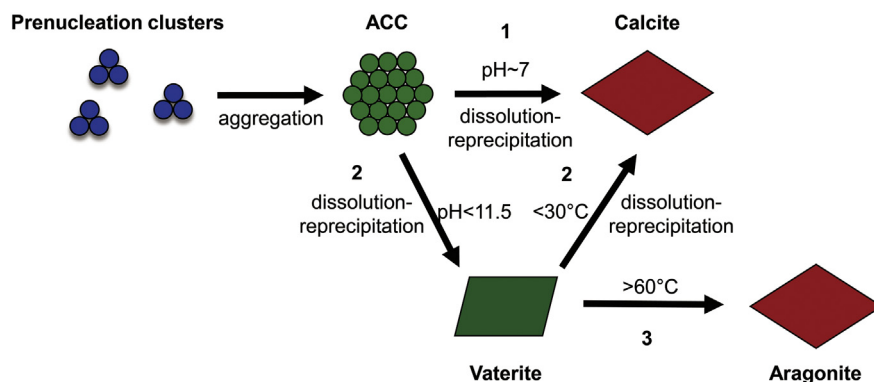

Fig. 7. Schematic representation of non-classical crystallization pathways of carbonate minerals. The figure was built after the descriptions of several previous works (Bots et al., 2012; Fernandez-Martinez et al., 2017; Rodriguez-Blanco et al., 2017).

Table 7
The calculated $^{26}Mg/^{24}Mg$ β factors of high-temperature minerals at B3LYP/6-31G* level.

Minerals	25 °C	100 °C	300 °C	600 °C	1000 °C
Forsterite_M1	1.02830	1.01843	1.00799	1.00348	1.00164
Forsterite_M2	1.02264	1.01467	1.00632	1.00275	1.00130
Average	1.02547	1.01655	1.00716	1.00311	1.00147
Spinel	1.03365	1.02197	1.00955	1.00416	1.00197
Diopside	1.02713	1.01760	1.00759	1.00330	1.00156
Enstatite_M1	1.02745	1.01783	1.00770	1.00335	1.00158
Enstatite_M2	1.02633	1.01717	1.00745	1.00324	1.00153
Average	1.02689	1.01750	1.00757	1.00329	1.00156
Tremolite_M1	1.02779	1.01807	1.00781	1.00339	1.00160
Tremolite_M2	1.02642	1.01714	1.00739	1.00321	1.00151
Tremolite_M3	1.02794	1.01816	1.00785	1.00341	1.00161
Average	1.02727	1.01771	1.00765	1.00332	1.00157
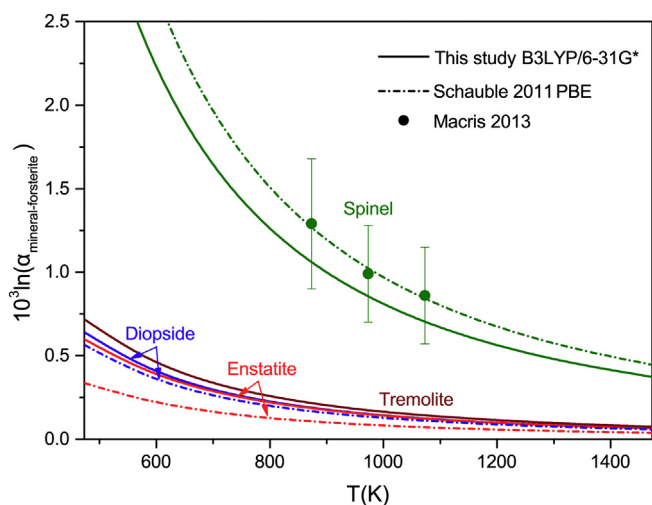
Fig. 8. Calculated $^{26}Mg/^{24}Mg$ fractionation factors for minerals relative to forsterite at B3LYP/6-31G* level. Previous experimental (Macris et al., 2013) and theoretical (Schauble, 2011) data are shown for comparison.
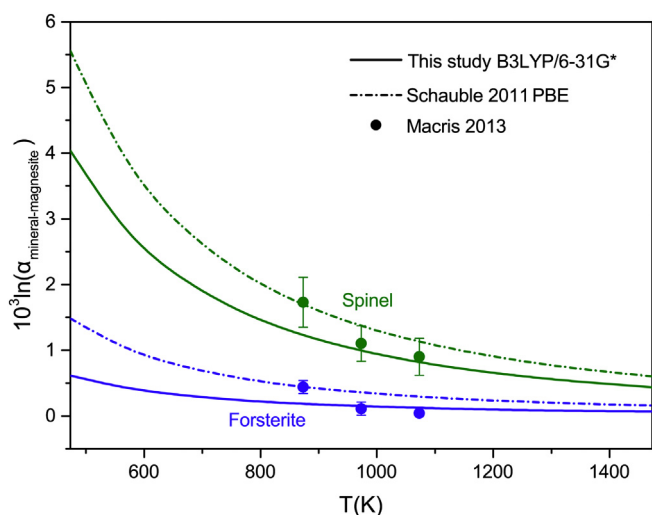

Fig. 9. Estimated $^{26}Mg/^{24}Mg$ fractionations for forsterite and spinel relative to magnesite. Previous theoretical (Schauble, 2011) and experimental (Macris et al., 2013) results are shown for comparison.

(0.86 $\pm$ 0.29‰ at 800 °C). For natural sample observations, two previous studies reported Mg isotope fractionation values of 0.88 $\pm$ 0.08‰ and 0.75 $\pm$ 0.02‰ (Young et al., 2009), 0.25‰–0.55‰ (Liu et al., 2011), respectively. Our results are within

the error range of experimental results (Fig. 8). Note that the experimental fractionations between spinel and forsterite were obtained by the combination of two experimental results, i.e., spinel vs. magnesite and forsterite vs. magnesite at 600, 700 and 800 °C (Macris et al., 2013). Both of them are slightly larger than our calculation results at low temperatures. However, as the temperature increases, the experimental results become increasingly closer to our results (Fig. 9).

The difference between experimental results and our calculations is possibly related to the pressure effect (Polyakov and Kharlashina, 1994), because the experiments in Macris et al. (2013) were all conducted at 1 GPa while the calculations here are done at 0 pressure. Generally, compression leads to the increase of β values. If the changes in β factors of two phases are not in the same magnitude, pressure effect will emerge. Huang et al. (2013) found that when pressure increases from 0 GPa to 3 GPa, the $^{26}Mg/^{24}Mg$ fractionation between clinopyroxene and pyrope (with Mg coordinate number of six and eight, respectively) will increases from 0.673‰ to 0.785‰ at 1200 K, while in the case of clinopyroxene and olivine (both with Mg coordinate number of six), almost no changes were found. In this study, Mg^{2+} is in 4-coordinated in spinel and in 6-coordinated in magnesite and forsterite, it is possible there is small pressure effect for spinel vs. magnesite and spinel vs. forsterite cases. Thus, this may explain why the calculated results for forsterite vs. magnesite are in good agreement with experimental results, while for spinel vs. magnesite and spinel vs. forsterite cases, our results are slightly smaller than those of experiments (Figs. 8 and 9).

Based on the predicted fractionations between spinel and forsterite, we find two possible explanations for the discrepancies between two observations of natural samples (Young et al., 2009; Liu et al., 2011). First, the estimated equilibrium pressures for San Carlos Group I inclusions range from 0.9 Gpa to 2.5 Gpa (Frey and Prinz, 1978) and the Kuandian peridotite xenoliths probably originated from upper mantle at the depth < 80 km (Wu et al., 2006). If only from the view of pressure effect, we find the results of Young et al. (2009), which are slightly larger than our prediction, are more reasonable. Second, both study of Liu et al. (2011) and Young et al. (2009) observed measurable $(Cr^{3+})^{VI}$ and $(Fe^{3+})^{VI}$ contents in their spinel samples. The substitution of $(Al^{3+})^{VI}$ by $(Cr^{3+})^{VI}$ and $(Fe^{3+})^{VI}$ in spinel will lower the β factor of spinel (Schauble, 2011). Liu et al. (2011) calculated the fractionation between spinel and olivine based on $Al^{3+}:Cr^{3+}:Fe^{3+}$ ratios of their samples, the results are close to our estimated fractionation. From this point of view, the results of Liu et al. (2011) are more reasonable. However, these two effects (pressure effects and cation substitution) are not fully understood, further investigations are needed to reveal their effects on Mg isotope partitioning in spinel.

5. Conclusion

Equilibrium Mg isotope fractionation factors of minerals and aqueous species are provided. The minerals are simulated by the VVCM method and the phonon-based periodic boundary method. The solvation effects are treated by the explicit-plus-implicit solvent model, including both short- and long-range effects. We find that configuration sampling is essential to obtain correct β factors of aqueous species. Both solids and aqueous species are found to be sensitive to theoretical levels, therefore, we suggest to use consistent theoretical levels for these phases.

The predicted Mg isotope fractionations between carbonates and aqueous Mg^{2+} are very close to those of a previous theoretical work (Pinilla et al., 2015). The Mg isotope fractionations between ACCs and solutions are calculated for the first time. ACCs have larger β factor than aqueous Mg^{2+}, e.g., about 1.45‰ heavier than solutions at room temperature. For brucite vs. aqueous Mg^{2+}, the fractionations at 25 °C are found as +2.7‰ and +2.9‰ by using B3LYP/6-31G* and B3LYP/6-311G* basis sets, respectively. The predicted fractionations have been systematically compared with the results of previous works. The

discrepancies between theoretical and experimental works may be caused by several factors, i.e., the existence of Mg-bearing species in experimental fluids, the incorporation of hydrated Mg^{2+} into the solids, the concentration effect, and the emergence of intermediate precursors (e.g., ACCs).

By applying VVCM to high-temperature phases, Mg isotope fractionations between several minerals are predicted. The predicted β factors for high-temperature phases are in the order of spinel > tremolite > diopside > enstatite > forsterite. For spinel vs. olivine, the origin of the discrepancies between previous observations of natural samples can be explained by the pressure effect or cation substitution.

Acknowledgments

Appendix A. Supplementary data

Supplementary data to this article can be found online at https://doi.org/10.1016/j.chemgeo.2018.04.005.

References

Akilan, C., Rohman, N., Hefter, G., Buchner, R., 2006. Temperature effects on ion association and hydration in $MgSO_4$ by dielectric spectroscopy. ChemPhysChem 7 (11), 2319–2330.

Baker, J.A., Schiller, M., Bizzarro, M., 2012. ^{26}Al-^{26}Mg deficit dating ultramafic meteorites and silicate planetesimal differentiation in the early Solar System? Geochim. Cosmochim. Acta 77, 415–431.

Becke, A.D., 1993. Density-functional thermochemistry. 3. The role of exact exchange. J. Chem. Phys. 98 (7), 5648–5652.

Bigeleisen, J., Mayer, M.G., 1947. Calculation of equilibrium constants for isotopic exchange reactions. J. Chem. Phys. 15 (5), 261–267.

Black, J.R., Yin, Q.-z, Casey, W.H., 2006. An experimental study of magnesium-isotope fractionation in chlorophyll-a photosynthesis. Geochim. Cosmochim. Acta 70 (16), 4072–4079.

Black, J.R., Yin, Q.-z, Rustad, J.R., Casey, W.H., 2007. Magnesium isotopic equilibrium in chlorophylls. J. Am. Chem. Soc. 129 (28) (8690–+).

Black, J.R., Epstein, E., Rains, W.D., Yin, Q.-Z., Casey, W.H., 2008. Magnesium-isotope fractionation during plant growth. Environ. Sci. Technol. 42 (21), 7831–7836.

Blanchard, M., Poitrasson, F., Meheut, M., Lazzeri, M., Mauri, F., Balan, E., 2009. Iron isotope fractionation between pyrite (FeS_2), hematite (Fe_2O_3) and siderite ($FeCO_3$): a first-principles density functional theory study. Geochim. Cosmochim. Acta 73 (21), 6565–6578.

Blanchard, M., Dauphas, N., Hu, M.Y., Roskosz, M., Alp, E.E., Golden, D.C., Sio, C.K., Tissot, F.L.H., Zhao, J., Gao, L., Morris, R.V., Fornace, M., Floris, A., Lazzeri, M., Balan, E., 2015. Reduced partition function ratios of iron and oxygen in goethite. Geochim. Cosmochim. Acta 151, 19–33.

Blanchard, M., Balan, E., Schauble, E.A., 2017. Equilibrium fractionation of non-traditional isotopes: a molecular modeling perspective. Rev. Mineral. Geochem. 82 (1), 27–63.

Bolou-Bi, E.B., Poszwa, A., Leyval, C., Vigier, N., 2010. Experimental determination of magnesium isotope fractionation during higher plant growth. Geochim. Cosmochim. Acta 74 (9), 2523–2537.

Bots, P., Benning, L.G., Rodriguez-Blanco, J.-D., Roncal-Herrero, T., Shaw, S., 2012. Mechanistic insights into the crystallization of amorphous calcium carbonate (ACC). Cryst. Growth Des. 12 (7), 3806–3814.

Brown, P.E., Bowman, J.R., Kelly, W.C., 1985. Petrologic and stable isotope constrains on the source and evolution of skarn-forming fluids at pine-creek, California. Econ. Geol. 80 (1), 72–95.

Buhl, D., Immenhauser, A., Smeulders, G., Kabiri, L., Richter, D.K., 2007. Time series delta ^{26}Mg analysis in speleothem calcite: kinetic versus equilibrium fractionation, comparison with other proxies and implications for palaeoclimate research. Chem. Geol. 244 (3–4), 715–729.

Cartwright, J.H.E., Checa, A.G., Gale, J.D., Gebauer, D., Sainz-Diaz, C.I., 2012. Calcium carbonate polymorphism and its role in biomineralization: how many amorphous calcium carbonates are there? Angew. Chem. Int. Ed. 51 (48), 11960–11970.

Chacko, T., Cole, D.R., Horita, J., 2001. Equilibrium oxygen, hydrogen and carbon isotope fractionation factors applicable to geologic systems. In: Valley, J.W., Cole, D.R. (Eds.), Stable Isotope Geochemistry. Reviews in Mineralogy & Geochemistry, pp. 1–81.

Chakoumakos, B.C., Loong, C.K., Schultz, A.J., 1997. Low-temperature structure and dynamics of brucite. J. Phys. Chem. B 101 (46), 9458–9462.

Clarkson, J.R., Price, T.J., Adams, C.J., 1992. Role of metastable phases in the spontaneous precipitation of calcium carbonate. J. Chem. Soc. Faraday Trans. 88 (2), 243–249.

Cobourne, G., Mountjoy, G., Rodriguez-Blanco, J.D., Benning, L.G., Hannon, A.C., Plaisier, J.R., 2014. Neutron and X-ray diffraction and empirical potential structure refinement modelling of magnesium stabilised amorphous calcium carbonate. J. Non-Cryst. Solids 401, 154–158.

Colla, C.A., Casey, W.H., André Ohlin, C., 2018. Computational prediction of Mg-isotope fractionation between aqueous $[Mg(OH_2)_6]^{2+}$ and brucite. Geochim. Cosmochim. Acta. http://dx.doi.org/10.1016/j.gca.2018.02.005. (In press).

Dauphas, N., Schauble, E.A., 2016. Mass fractionation laws, mass-independent effects, and isotopic anomalies. In: Jeanloz, R., Freeman, K.H. (Eds.), Annual Review of Earth and Planetary Sciences. Vol 44. pp. 709–783.

Davis, A.M., Richter, F.M., Mendybaev, R.A., Janney, P.E., Wadhwa, M., McKeegan, K.D., 2015. Isotopic mass fractionation laws for magnesium and their effects on ^{26}Al-^{26}Mg systematics in solar system materials. Geochim. Cosmochim. Acta 158, 245–261.

Dawson, P., Hadfield, C.D., Wilkinson, G.R., 1973. The polarized infra-red and Raman spectra of $Mg(OH)_2$ and $Ca(OH)_2$. J. Phys. Chem. Solids 34 (7), 1217–1225.

Demichelis, R., Raiteri, P., Gale, J.D., Quigley, D., Gebauer, D., 2011. Stable prenucleation mineral clusters are liquid-like ionic polymers. Nat. Commun. 2, 590.

Demichelis, R., Raiteri, P., Gale, J.D., 2017. Ab initio modelling of the structure and properties of crystalline calcium carbonate. In: Van Driessche, A.E.S., Kellermeier, M., Benning, L.G., Gebauer, D. (Eds.), New Perspectives on Mineral Nucleation and Growth: From Solution Precursors to Solid Materials. Springer International Publishing, Cham, pp. 113–135.

Di Tommaso, D., de Leeuw, N.H., 2010a. First principles simulations of the structural and dynamical properties of hydrated metal ions me^{2+} and solvated metal carbonates (Me = Ca, Mg, and Sr). Cryst. Growth Des. 10 (10), 4292–4302.

Di Tommaso, D., de Leeuw, N.H., 2010b. Structure and dynamics of the hydrated magnesium ion and of the solvated magnesium carbonates: insights from first principles simulations. Phys. Chem. Chem. Phys. 12 (4), 894–901.

Fantle, M.S., Higgins, J., 2014. The effects of diagenesis and dolomitization on Ca and Mg isotopes in marine platform carbonates: implications for the geochemical cycles of Ca and Mg. Geochim. Cosmochim. Acta 142, 458–481.

Fernandez-Martinez, A., Lopez-Martinez, H., Wang, D., 2017. Structural Characteristics and the Occurrence of Polymorphism in Amorphous Calcium Carbonate. Springer International Publishing, Cham, pp. 77-92.

Feynman, R.P., 1939. Forces in molecules. Phys. Rev. 56 (4), 340–343.

Finch, A.A., Allison, N., 2007. Coordination of Sr and Mg in calcite and aragonite. Mineral. Mag. 71 (5), 539–552.

Frey, F.A., Prinz, M., 1978. Ultramafic inclusions from San-Carlos, Arizona - petrologic and geochemical data bearing on their petrogenesis. Earth Planet. Sci. Lett. 38 (1), 129–176.

Frisch, M.J., Trucks, G.W., Schlegel, H.B., Scuseria, G.E., Robb, M.A., Cheeseman, J.R., Scalmani, G., Barone, V., Mennucci, B., Petersson, G.A., Nakatsuji, H., Caricato, M., Li, X., Hratchian, H.P., Izmaylov, A.F., Bloino, J., Zheng, G., Sonnenberg, J.L., Hada, M., Ehara, M., Toyota, K., Fukuda, R., Hasegawa, J., Ishida, M., Nakajima, T., Honda, Y., Kitao, O., Nakai, H., Vreven, T., Montgomery, J.A., Peralta Jr., J.E., Ogliaro, F., Bearpark, M., Heyd, J.J., Brothers, E., Kudin, K.N., Staroverov, V.N., Keith, T., Kobayashi, R., Normand, J., Raghavachari, K., Rendell, A., Burant, J.C., Iyengar, S.S., Tomasi, J., Cossi, M., Rega, N., Millam, J.M., Klene, M., Knox, J.E., Cross, J.B., Bakken, V., Adamo, C., Jaramillo, J., Comperts, R., Stratmann, R.E., Yazyev, O., Austin, A.J., Cammi, R., Pomelli, C., Ochterski, J.W., Martin, R.L., Morokuma, K., Zakrzewski, V.G., Voth, G.A., Salvador, P., Dannenberg, J.J., Dapprich, S., Daniels, A.D., Farkas, O., Foresman, J.B., Ortiz, J.V., Cioslowski, J., Fox, D.J., 2013. Gaussian 09, (Reversion D.01). Gaussian, Inc., Wallingford CT.

Fujii, T., Moynier, F., Dauphas, N., Abe, M., 2011. Theoretical and experimental investigation of nickel isotopic fractionation in species relevant to modern and ancient oceans. Geochim. Cosmochim. Acta 75 (2), 469–482.

Fujii, T., Moynier, F., Abe, M., Nemoto, K., Albarède, F., 2013. Copper isotope fractionation between aqueous compounds relevant to low temperature geochemistry and biology. Geochim. Cosmochim. Acta 110, 29–44.

Gagnon, A.C., Depaolo, D.J., Deyoreo, J.J., 2010. Calcium Isotope Signature of Amorphous Calcium Carbonate: A Probe of Crystallization Pathway? In: AGU Fall Meeting Abstracts.

Galy, A., Young, E.D., Ash, R.D., O'Nions, R.K., 2000. The formation of chondrules at high gas pressures in the solar nebula. Science 290 (5497), 1751–1753.

Gebauer, D., Voelkel, A., Coelfen, H., 2008. Stable prenucleation calcium carbonate clusters. Science 322 (5909), 1819–1822.

Geske, A., Lokier, S., Dietzel, M., Richter, D.K., Buhl, D., Immenhauser, A., 2015. Magnesium isotope composition of sabkha porewater and related (sub-) recent stoichiometric dolomites, Abu Dhabi (UAE). Chem. Geol. 393-394, 112–124.

Gibbs, G.V., 1982. Molecules as models for bonding in silicates. Am. Mineral. 67 (5–6), 421–450.

Giuffre, A.J., Gagnon, A.C., De Yoreo, J.J., Dove, P.M., 2015. Isotopic tracer evidence for the amorphous calcium carbonate to calcite transformation by dissolution–reprecipitation. Geochim. Cosmochim. Acta 165, 407–417.

Goodwin, A.L., Michel, F.M., Phillips, B.L., Keen, D.A., Dove, M.T., Reeder, R.J., 2010. Nanoporous structure and medium-range order in synthetic amorphous calcium carbonate. Chem. Mater. 22 (10), 3197–3205.

Handler, M.R., Baker, J.A., Schiller, M., Bennett, V.C., Yaxley, G.M., 2009. Magnesium stable isotope composition of Earth's upper mantle. Earth Planet. Sci. Lett. 282 (1–4), 306–313.

Harder, H., 1972. The role of magnesium in the formation of smectite minerals. Chem. Geol. 10 (1), 31–39.

He, H.-t, Liu, Y., 2015. Silicon isotope fractionation during the precipitation of quartz and the adsorption of H₄SiO₄(aq) on Fe(III)-oxyhydroxide surfaces. Chin. J. Geochem. 34 (4), 459–468.

He, M., Liu, X., Lu, X., Wang, R., 2016. Molecular simulation study on K⁺–Cl⁻ ion pair in geological fluids. Acta Geochim. 36 (1), 1–8.

He, H.-t, Zhang, S.T., Zhu, C., Liu, Y., 2016. Equilibrium and kinetic Si isotope fractionation factors and their implications for Si isotope distributions in the Earth's surface environments. Acta Geochimica 35 (1), 15–24.

Head-Gordon, M., Pople, J.A., Frisch, M.J., 1988. MP2 energy evaluation by direct methods. Chem. Phys. Lett. 153 (6), 503–506.

Hellwege, K.H., Lesch, W., Plihal, M., Schaack, G., 1970. Zwei-Phononen-Absorptionsspektren und Dispersion der Schwingungszweige in Kristallen der Kalkspatstruktur. Z. Phys. 232 (1), 61–86.

Higgins, J.A., Schrag, D.P., 2010. Constraining magnesium cycling in marine sediments using magnesium isotopes. Geochim. Cosmochim. Acta 74 (17), 5039–5053.

Huang, F., Zhang, Z., Lundstrom, C.C., Zhi, X., 2011. Iron and magnesium isotopic compositions of peridotite xenoliths from Eastern China. Geochim. Cosmochim. Acta 75 (12), 3318–3334.

Huang, K.-J., Teng, F.-Z., Wei, G.-J., Ma, J.-L., Bao, Z.-Y., 2012. Adsorption- and desorption-controlled magnesium isotope fractionation during extreme weathering of basalt in Hainan Island, China. Earth Planet. Sci. Lett. 359, 73–83.

Huang, F., Chen, L., Wu, Z., Wang, W., 2013. First-principles calculations of equilibrium Mg isotope fractionations between garnet, clinopyroxene, orthopyroxene, and olivine: implications for Mg isotope thermometry. Earth Planet. Sci. Lett. 367, 61–70.

Huang, F., Wu, Z., Huang, S., Wu, F., 2014. First-principles calculations of equilibrium silicon isotope fractionation among mantle minerals. Geochim. Cosmochim. Acta 140, 509–520.

Immenhauser, A., Buhl, D., Richter, D., Niedermayr, A., Riechelmann, D., Dietzel, M., Schulte, U., 2010. Magnesium-isotope fractionation during low-Mg calcite precipitation in a limestone cave – field study and experiments. Geochim. Cosmochim. Acta 74 (15), 4346–4364.

Kapitán, J., Dracínský, M., Kamínský, J., Benda, L., Bour, P., 2010. Theoretical modeling of magnesium ion imprints in the Raman scattering of water. J. Phys. Chem. B 114 (10), 3574–3582.

Kieffer, S.W., 1982. Thermodynamics and lattice-vibrations of minerals. 5. Applications to phase-equilibria, isotopic fractionation, and high-pressure thermodynamic properties. Rev. Geophys. 20 (4), 827–849.

Klamt, A., Schuurmann, G., 1993. COSMO - a new approach to dielectric screening in solvents with explicit expressions for the screening energy and its gradient. J. Chem. Soc. Perkin Trans. 2 (5), 799–805.

Kresse, G., Furthmüller, J., 1996. Efficiency of ab-initio total energy calculations for metals and semiconductors using a plane-wave basis set. Comput. Mater. Sci. 6 (1), 15–50.

Lee, C.T., Yang, W.T., Parr, R.G., 1988. Development of the Colle-Salvetti correlation-energy formula into a function of the electron-density. Phys. Rev. B 37 (2), 785–789.

Li, X.F., Liu, Y., 2010. First-principles study of Ge isotope fractionation during adsorption onto Fe(III)-oxyhydroxide surfaces. Chem. Geol. 278 (1–2), 15–22.

Li, X.F., Liu, Y., 2011. Equilibrium se isotope fractionation parameters: a first-principles study. Earth Planet. Sci. Lett. 304 (1–2), 113–120.

Li, X.F., Liu, Y., 2015. A theoretical model of isotopic fractionation by thermal diffusion and its implementation on silicate melts. Geochim. Cosmochim. Acta 154, 18–27.

Li, X.F., Zhao, H., Tang, M., Liu, Y., 2009. Theoretical prediction for several important equilibrium Ge isotope fractionation factors and geological implications. Earth Planet. Sci. Lett. 287 (1–2), 1–11.

Li, W., Chakraborty, S., Beard, B.L., Romanek, C.S., Johnson, C.M., 2012. Magnesium isotope fractionation during precipitation of inorganic calcite under laboratory conditions. Earth Planet. Sci. Lett. 333-334, 304–316.

Li, W., Beard, B.L., Li, C., Johnson, C.M., 2014. Magnesium isotope fractionation between brucite [Mg(OH)₂] and Mg aqueous species: implications for silicate weathering and biogeochemical processes. Earth Planet. Sci. Lett. 394, 82–93.

Li, W., Beard, B.L., Li, C., Xu, H., Johnson, C.M., 2015. Experimental calibration of Mg isotope fractionation between dolomite and aqueous solution and its geological implications. Geochim. Cosmochim. Acta 157, 164–181.

Lin, C.-J., Yang, S.-Y., Huang, S.-J., Chan, J.C.C., 2015. Structural characterization of Mg-stabilized amorphous calcium carbonate by Mg-25 solid-state NMR spectroscopy. J. Phys. Chem. C 119 (13), 7225–7233.

Liu, Y., 2013. In: On the test of a new volume variable cluster model method for stable isotopic fractionation of solids: equilibrium Mg isotopic fractionations between minerals and solutions. Goldschmidt 2013 Conference Abstracts. 1632 (abstr.).

Liu, Y., Tossell, J.A., 2005. Ab initio molecular orbital calculations for boron isotope fractionations on boric acids and borates. Geochim. Cosmochim. Acta 69 (16), 3995–4006.

Liu, S.-A., Teng, F.-Z., He, Y., Ke, S., Li, S., 2010. Investigation of magnesium isotope fractionation during granite differentiation: implication for mg isotopic composition of the continental crust. Earth Planet. Sci. Lett. 297 (3–4), 646–654.

Liu, Q., Tossell, J.A., Liu, Y., 2010. On the proper use of the Bigeleisen–Mayer equation and corrections to it in the calculation of isotopic fractionation equilibrium constants. Geochim. Cosmochim. Acta 74 (24), 6965–6983.

Liu, S.-A., Teng, F.-Z., Yang, W., Wu, F.-Y., 2011. High-temperature inter-mineral magnesium isotope fractionation in mantle xenoliths from the North China craton. Earth Planet. Sci. Lett. 308 (1–2), 131–140.

Macris, C.A., Young, E.D., Manning, C.E., 2013. Experimental determination of equilibrium magnesium isotope fractionation between spinel, forsterite, and magnesite from 600 to 800 degrees C. Geochim. Cosmochim. Acta 118, 18–32.

Markham, G.D., Glusker, J.P., Bock, C.W., 2002. The arrangement of first- and second-sphere water molecules in divalent magnesium complexes: results from molecular orbital and density functional theory and from structural crystallography. J. Phys. Chem. B 106 (19), 5118–5134.

Mavromatis, V., Gautier, Q., Bosc, O., Schott, J., 2013. Kinetics of Mg partition and Mg stable isotope fractionation during its incorporation in calcite. Geochim. Cosmochim. Acta 114, 188–203.

Mavromatis, V., et al., 2017. Impact of amorphous precursor phases on magnesium isotope signatures of Mg-calcite. Earth Planet. Sci. Lett. 464, 227–236.

Meheut, M., Schauble, E.A., 2014. Silicon isotope fractionation in silicate minerals: insights from first-principles models of phyllosilicates, albite and pyrope. Geochim. Cosmochim. Acta 134, 137–154.

Meheut, M., Lazzeri, M., Balan, E., Mauri, F., 2007. Equilibrium isotopic fractionation in the kaolinite, quartz, water system: prediction from first-principles density-functional theory. Geochim. Cosmochim. Acta 71 (13), 3170–3181.

Meheut, M., Lazzeri, M., Balan, E., Mauri, F., 2009. Structural control over equilibrium silicon and oxygen isotopic fractionation: a first-principles density-functional theory study. Chem. Geol. 258 (1–2), 28–37.

Meheut, M., Lazzeri, M., Balan, E., Mauri, F., 2010. First-principles calculation of H/D isotopic fractionation between hydrous minerals and water. Geochim. Cosmochim. Acta 74 (14), 3874–3882.

Mink, J., Németh, C., Hajba, L., Sandström, M., Goggin, P.L., 2003. Infrared and Raman spectroscopic and theoretical studies of hexaaqua metal ions in aqueous solution. J. Mol. Struct. 661-662, 141–151.

Nicola, J.H., Scott, J.F., Couto, R.M., Correa, M.M., 1976. Raman spectra of dolomite [CaMg(CO₃)₂]. Phys. Rev. B 14 (10), 4676–4678.

Ogino, T., Suzuki, T., Sawada, K., 1987. The formation and transformation mechanism of calcium-carbonate in water. Geochim. Cosmochim. Acta 51 (10), 2757–2767.

Ohtaki, H., Radnai, T., 1993. Structure and dynamics of hydrated ions. Chem. Rev. 93 (3), 1157–1204.

Oi, T., Yanase, S., 2001. Calculations of reduced partition function ratios of hydrated monoborate anion by the ab initio molecular orbital theory. J. Nucl. Sci. Technol. 38 (6), 429–432.

Oneil, J.R., 1986. Theoretical and experimental aspects of isotopic fractionation. Rev. Mineral. 16, 1–40.

Palinkas, G., Radnai, T., Dietz, W., Szasz, G.I., Heinzinger, K., 1982. Hydration shell structures in an MgCl₂ solution from X-ray and MD studies. Z. Naturforsch. A J. Phys. Sci. 37 (9), 1049–1060.

Pearce, C.R., Saldi, G.D., Schott, J., Oelkers, E.H., 2012. Isotopic fractionation during congruent dissolution, precipitation and at equilibrium: evidence from Mg isotopes. Geochim. Cosmochim. Acta 92, 170–183.

Perdew, J.P., Burke, K., Ernzerhof, M., 1996. Generalized gradient approximation made simple. Phys. Rev. Lett. 77 (18), 3865–3868.

Pilati, T., Demartin, F., Gramaccioli, C.M., 1998. Lattice-dynamical estimation of atomic displacement parameters in carbonates: calcite and aragonite CaCO₃, dolomite CaMg (CO₃)₂ and magnesite MgCO₃. Acta Crystallogr. Sect. B: Struct. Sci. Cryst. Eng. Mater. 54, 515–523.

Pinilla, C., Blanchard, M., Balan, E., Natarajan, S.K., Vuilleumier, R., Mauri, F., 2015. Equilibrium magnesium isotope fractionation between aqueous Mg²⁺ and carbonate minerals: insights from path integral molecular dynamics. Geochim. Cosmochim. Acta 163, 126–139.

Pogge von Strandmann, P.A.E., Elliot, T., Marschall, H.R., Coath, C., Lai, Y.-J., Jeffcoate, A., Ionov, D., 2011. Variations of Li and Mg isotope ratios in bulk chondrites and mantle xenoliths. Geochim. Cosmochim. Acta 75 (18), 5247–5268.

Polyakov, V.B., Kharlashina, N.N., 1994. Effect of pressure on equilibrium isotopic fractionation. Geochim. Cosmochim. Acta 58 (21), 4739–4750.

Pouget, E.M., Bomans, P.H.H., Goos, J.A.C.M., Frederik, P.M., With, G.D., Sommerdijk, N.A.J.M., 2009. The initial stages of template-controlled CaCO3 formation revealed by Cryo-TEM. Science 323 (5920), 1455–1458.

Purgstaller, B., Mavromatis, V., Immenhauser, A., Dietzel, M., 2016. Transformation of Mg-bearing amorphous calcium carbonate to Mg-calcite – in situ monitoring. Geochim. Cosmochim. Acta 174, 180–195.

Purgstaller, B., Konrad, F., Dietzel, M., Immenhauser, A., Mavromatis, V., 2017. Control of Mg²⁺/Ca²⁺ activity ratio on the formation of crystalline carbonate minerals via an amorphous precursor. Cryst. Growth Des. 17 (3), 1069–1078.

Radha, A.V., Fernandez-Martinez, A., Hu, Y., Jun, Y.S., Waychunas, G.A., Navrotsky, A., 2012. Energetic and structural studies of amorphous Ca₁₋ₓMgₓCO₃·nH₂O (0 ≤ x ≤ 1). Geochim. Cosmochim. Acta 90, 83–95.

Raiteri, P., Gale, J.D., 2010. Water is the key to nonclassical nucleation of amorphous calcium carbonate. J. Am. Chem. Soc. 132 (49), 17623–17634.

Redlich, O., 1935. A general relationship between the oscillation frequency of isotropic molecules (with remarks on the calculation of harmonious force constants). Z. Phys. Chem. B 28 (5), 371–382.

Richet, P., Bottinga, Y., Javoy, M., 1977. Review of hydrogen, carbon, nitrogen, oxygen, sulfur and chlorine stable isotope fractionation among gaseous molecules. Annu. Rev. Earth Planet. Sci. 5, 65–110.

Rodriguez-Blanco, J.D., Shaw, S., Benning, L.G., 2011. The kinetics and mechanisms of amorphous calcium carbonate (ACC) crystallization to calcite, via vaterite. Nano 3 (1), 265–271.

Rodriguez-Blanco, J.D., Shaw, S., Bots, P., Roncal-Herrero, T., Benning, L.G., 2012. The role of pH and Mg on the stability and crystallization of amorphous calcium carbonate. J. Alloys Compd. 536, S477–S479.

Rodriguez-Blanco, J.D., Shaw, S., Benning, L.G., 2015. A route for the direct

crystallization of dolomite. Am. Mineral. 100 (5–6), 1172–1181.

Rodriguez-Blanco, J.D., Sand, K.K., Benning, L.G., 2017. ACC and Vaterite as intermediates in the solution-based crystallization of CaCO$_3$. In: Van Driessche, A.E.S., Kellermeier, M., Benning, L.G., Gebauer, D. (Eds.), New Perspectives on Mineral Nucleation and Growth: From Solution Precursors to Solid Materials. Springer International Publishing, Cham, pp. 93–111.

Ross, N.L., 1997. The equation of state and high-pressure behavior of magnesite. Am. Mineral. 82 (7–8), 682–688.

Ross, N.L., Reeder, R.J., 1992. High-pressure structural study of dolomite and ankerite. Am. Mineral. 77 (3–4), 412–421.

Rustad, J.R., Dixon, D.A., 2009. Prediction of iron-isotope fractionation between hematite (α-Fe2O3) and ferric and ferrous Iron in aqueous solution from density functional theory. J. Phys. Chem. A, 113(44): 12249–12255.

Rustad, J.R., Nelmes, S.L., Jackson, V.E., Dixon, D.A., 2008. Quantum-chemical calculations of carbon-isotope fractionation in CO$_2$(g), aqueous carbonate species, and carbonate minerals. J. Phys. Chem. A 112 (3), 542–555.

Rustad, J.R., Casey, W.H., Yin, Q.-Z., Bylaska, E.J., Felmy, A.R., Bogatko, S.A., Jackson, V.E., Dixon, D.A., 2010. Isotopic fractionation of Mg^{2+}(aq), Ca^{2+}(aq), and Fe^{2+}(aq) with carbonate minerals. Geochim. Cosmochim. Acta 74 (22), 6301–6323.

Rutt, H.N., Nicola, J.H., 1974. Raman spectra of carbonates of calcite structure. J. Phys. C Solid State 7(24): 4522–4528.

Saenger, C., Wang, Z., 2014. Magnesium isotope fractionation in biogenic and abiogenic carbonates: implications for paleoenvironmental proxies. Quat. Sci. Rev. 90, 1–21.

Saulnier, S., Rollion-Bard, C., Vigier, N., Chaussidon, M., 2012. Mg isotope fractionation during calcite precipitation: an experimental study. Geochim. Cosmochim. Acta 91, 75–91.

Schauble, E.A., 2004. Applying stable isotope fractionation theory to new systems. In: Johnson, C.M., Beard, B.L., Albarede, F. (Eds.), Geochemistry of Non-Traditional Stable Isotopes. Reviews in Mineralogy & Geochemistry, pp. 65–111.

Schauble, E.A., 2011. First-principles estimates of equilibrium magnesium isotope fractionation in silicate, oxide, carbonate and hexaaquamagnesium(2 +) crystals. Geochim. Cosmochim. Acta 75 (3), 844–869.

Schauble, E.A., Ghosh, P., Eiler, J.M., 2006. Preferential formation of ^{13}C–^{18}O bonds in carbonate minerals, estimated using first-principles lattice dynamics. Geochim. Cosmochim. Acta 70 (10), 2510–2529.

Schott, J., Mavromatis, V., Fujii, T., Pearce, C.R., Oelkers, E.H., 2016. The control of carbonate mineral Mg isotope composition by aqueous speciation: theoretical and experimental modeling. Chem. Geol. 445, 120–134.

Shen, B., Jacobsen, B., Lee, C.T., Yin, Q.Z., Morton, D.M., 2009. The Mg isotopic systematics of granitoids in continental arcs and implications for the role of chemical weathering in crust formation. Proc. Natl. Acad. Sci. U. S. A. 106 (49), 20652–20657.

Singer, J.W., Yazaydin, A.Ö., Kirkpatrick, R.J., Bowers, G.M., 2012. Structure and transformation of amorphous calcium carbonate: a solid-State ^{43}Ca NMR and computational molecular dynamics investigation. Chem. Mater. 24 (10), 1828–1836.

Stefánsson, A., Lemke, K.H., Bénézeth, P., Schott, J., 2017. Magnesium bicarbonate and carbonate interactions in aqueous solutions: an infrared spectroscopic and quantum chemical study. Geochim. Cosmochim. Acta 198, 271–284.

Teng, F.-Z., 2017. Magnesium Isotope Geochemistry. Rev. Mineral. Geochem. 82 (1), 219–287.

Teng, F.-Z., Wadhwa, M., Helz, R.T., 2007. Investigation of magnesium isotope fractionation during basalt differentiation: implications for a chondritic composition of the terrestrial mantle. Earth Planet. Sci. Lett. 261 (1–2), 84–92.

Teng, F.-Z., Li, W.-Y., Rudnick, R.L., Gardner, L.R., 2010. Contrasting lithium and magnesium isotope fractionation during continental weathering. Earth Planet. Sci. Lett.

300 (1–2), 63–71.

Tipper, E., Galy, A., Bickle, M., 2006. Riverine evidence for a fractionated reservoir of Ca and Mg on the continents: implications for the oceanic Ca cycle. Earth Planet. Sci. Lett. 247 (3–4), 267–279.

Tipper, E.T., Calmels, D., Gaillardet, J., Louvat, P., Capmas, F., Dubacq, B., 2012a. Positive correlation between Li and Mg isotope ratios in the river waters of the Mackenzie Basin challenges the interpretation of apparent isotopic fractionation during weathering. Earth Planet. Sci. Lett. 333-334, 35–45.

Tipper, E.T., Lemarchand, E., Hindshaw, R.S., Reynolds, B.C., Bourdon, B., 2012b. Seasonal sensitivity of weathering processes: hints from magnesium isotopes in a glacial stream. Chem. Geol. 312, 80–92.

Togo, A., Tanaka, I., 2015. First principles phonon calculations in materials science. Scr. Mater. 108, 1–5.

Tomasi, J., Mennucci, B., Cammi, R., 2005. Quantum mechanical continuum solvation models. Chem. Rev. 105 (8), 2999–3093.

Urey, H.C., 1947. The thermodynamic properties of isotopic substances. J. Chem. Soc. 562–581 (MAY).

Wallace, A.F., et al., 2013. Microscopic evidence for liquid-liquid separation in supersaturated CaCO$_3$ solutions. Science 341 (6148), 885–889.

Wang, D., Hamm, L.M., Giuffre, A.J., Echigo, T., Rimstidt, J.D., Yoreo, J.J.D., et al., 2012. Revisiting geochemical controls on patterns of carbonate deposition through the lens of multiple pathways to mineralization. Faraday Discuss. 159 (0), 371–386.

Wang, Z., Hu, P., Gaetani, G., Liu, C., Saenger, C., Cohen, A., et al., 2013. Experimental calibration of Mg isotope fractionation between aragonite and seawater. Geochim. Cosmochim. Acta 102, 113–123.

Wang, W., Qin, T., Zhou, C., Huang, S., Wu, Z., Huang, F., 2017. Concentration effect on equilibrium fractionation of Mg-Ca isotopes in carbonate minerals: insights from first-principles calculations. Geochim. Cosmochim. Acta 208.

Wiechert, U., Halliday, A.N., 2007. Non-chondritic magnesium and the origins of the inner terrestrial planets. Earth Planet. Sci. Lett. 256 (3–4), 360–371.

Wimpenny, J., Colla, C.A., Yin, Q.-Z., Rustad, J.R., Casey, W.H., 2014. Investigating the behaviour of Mg isotopes during the formation of clay minerals. Geochim. Cosmochim. Acta 128, 178–194.

Wu, F.-Y., Walker, R.J., Yang, Y.-H., Yuan, H.-L., Yang, J.-H., 2006. The chemical-temporal evolution of lithospheric mantle underlying the North China Craton. Geochim. Cosmochim. Acta 70 (19), 5013–5034.

Wu, Z., Huang, F., Huang, S., 2015. Isotope fractionation induced by phase transformation: first-principles investigation for Mg$_2$SiO$_4$. Earth Planet. Sci. Lett. 409, 339–347.

Xantheas, S.S., 1995. Ab initio studies of cyclic water clusters (H$_2$O)n, n = 1–6. III. Comparison of density functional with MP2 results. J. Chem. Phys. 102 (11), 4505–4517.

Xiao, Y., Teng, F.-Z., Zhang, H.-F., Yang, W., 2013. Large magnesium isotope fractionation in peridotite xenoliths from eastern North China craton: product of melt-rock interaction. Geochim. Cosmochim. Acta 115, 241–261.

Yang, W., Teng, F.-Z., Zhang, H.-F., 2009. Chondritic magnesium isotopic composition of the terrestrial mantle: a case study of peridotite xenoliths from the North China craton. Earth Planet. Sci. Lett. 288 (3–4), 475–482.

Young, E.D., Tonui, E., Manning, C.E., Schauble, E., Macris, C.A., 2009. Spinel–olivine magnesium isotope thermometry in the mantle and implications for the Mg isotopic composition of Earth. Earth Planet. Sci. Lett. 288 (3–4), 524–533.

Young, E.D., Manning, C.E., Schauble, E.A., Shahar, A., Macris, C.A., Lazar, C., Jordan, M., 2015. High-temperature equilibrium isotope fractionation of non-traditional stable isotopes: experiments, theory, and applications. Chem. Geol. 395, 176–195.